Coupled CO_2-well-reservoir simulation using a partitioned approach: Effect of reservoir properties on well dynamics

Svend Tollak Munkejord*, Morten Hammer, Åsmund Ervik, Lars Hov Odsæter, Halvor Lund

SINTEF Energy Research, P.O. Box 4761 Torgarden, NO-7465 Trondheim, Norway

Abstract

We present a model framework for dynamic simulation of the flow of CO_2 and other components in an injection well coupled with a near-well reservoir. With a partitioned approach, we employ numerical methods adapted to the governing equations in each domain. In both the well and the reservoir, accurate thermodynamics are used. This model can be used for various design and operational considerations for CO_2-injection wells, i.e., the quantification of pressure and temperature transients, and phase composition, including the appearance of a water-rich phase.

We study cases where the flow in the well and the near-well reservoir are dynamically coupled. The rock properties are seen to strongly affect the well dynamics, both regarding magnitude and transient evolution of the bottomhole pressure. We consider a variation of this case where water is co-injected with CO_2, showing that this is a potential method to mitigate salt precipitation. We also consider intermittent injection, representing the case of direct injection from ships transporting CO_2. Finally, we observe that in the present cases, a coupled model (as opposed to a well-only model) is necessary in order to capture the dynamics in the well during injection.

Keywords: carbon dioxide, CO_2 injection, well, reservoir, CFD, fluid dynamics, thermodynamics

*Corresponding author.
Email address: svend.t.munkejord [a] sintef.no (Svend Tollak Munkejord)

This is the accepted version of an article published in Greenhouse Gases: Science and Technology
http://dx.doi.org/10.1002/ghg.2035

Nomenclature

Latin letters

d	Diameter	m
e	Specific internal energy	$\mathrm{J\,kg^{-1}}$
$\hat{e}$	Total specific energy	$\mathrm{J\,kg^{-1}}$
f	(Darcy) friction factor	1
f_π	Fractional flow function, see (11)	1
$\boldsymbol{F}$	Vector function	1
$\mathcal{F}$	Friction force	$\mathrm{N\,m^{-3}}$
g	Gravitational acceleration	$\mathrm{m\,s^{-2}}$
h	Specific enthalpy	$\mathrm{J\,kg^{-1}}$
h_i	Heat-transfer coefficient, (5)	$\mathrm{W\,m^{-2}\,K^{-1}}$
K	Permeability	$\mathrm{m^2}$
k_r	Relative permeability	1
l_y	Height	m
m_j	Mass of component j per volume	$\mathrm{kg\,m^{-3}}$
$\dot{m}$	Mass flux	$\mathrm{kg\,m^{-2}\,s^{-1}}$
P	Pressure	Pa
$\boldsymbol{Q}$	Heat flux per volume	$\mathrm{W\,m^{-3}}$
r	Radius	m
Re	Reynolds number	1
s	Skin factor	1
$\mathcal{S}$	Volume flow, see (13), (20)	$\mathrm{m^3\,s^{-1}}$
t	Time	s
T	Temperature	K
u	Velocity	$\mathrm{m\,s^{-1}}$
$\boldsymbol{U}$	Vector of unknowns	1
V	Volume	$\mathrm{m^3}$
w	Darcy flux	$\mathrm{m\,s^{-1}}$
x	Spatial coordinate	m
y	Depth	m
$\bar{y}$	Elevation	m
z	Mass fraction	$\mathrm{kg\,kg^{-1}}$

Greek letters

α	Volume fraction (saturation)	$\mathrm{m^3\,m^{-3}}$
ϕ	Porosity	1
γ	Prefactor in (23)	$\mathrm{m^3\,s^{-1}\,Pa^{-1}}$
λ	Mobility	$\mathrm{m\,s\,kg^{-1}}$
Λ	Well index	$\mathrm{m^3}$
μ	Dynamic viscosity	$\mathrm{kg\,m^{-1}\,s^{-1}}$
Φ	Coefficient in (4)	1
ρ	(Mass) density	$\mathrm{kg\,m^{-3}}$
ϱ	Mass flow rate per volume	$\mathrm{kg\,s^{-1}\,m^{-3}}$

Subscripts

bg Background
c CO_2
i Interfacial or inner
i Cell i

This is the accepted version of an article published in Greenhouse Gases: Science and Technology
http://dx.doi.org/10.1002/ghg.2035

j Component j
m Multiphase mixture
$\|$ Axial direction
π Phase π
R Reservoir
w Wall
w Water
wb Wellbore

Superscripts
n Time step n

Abbreviations
CCS CO_2 capture & storage
CFL Courant–Friedrichs–Lewy
EOS Equation of state
ImPEM Implicit pressure explicit mass

This is the accepted version of an article published in Greenhouse Gases: Science and Technology
http://dx.doi.org/10.1002/ghg.2035

1. Introduction

For CO_2 transport, pipelines are often cited as the most efficient alternative. However, CO_2 transport by ship is being considered for CO_2 sources close to the coast and far from an offshore storage site. In the early phases of CCS deployment, transported CO_2 quantities will be small, which makes ships the most cost-efficient means of transport. Ship transport will also be flexible in the sense that new sources can easily be added [see e.g. 1, 2]. For a ship-transport system, the arrival of ships may lead to intermittent injection introducing dynamics in the receiving system, well and reservoir, whereas in a pipeline system, the CO_2 supply may vary due to varying production. Such dynamics could have operational consequences and should be taken into account by models describing the flow at the transport-storage interface. In addition, possible processing at the injection site, well-flow dynamics [3], well integrity [4] and the response of the CO_2 storage reservoir need to be described. This requires good knowledge of the relevant CO_2-rich fluid properties, as well as the flow in the well and coupling between well and near-well flow, the interaction of brine and CO_2, etc. [5].

Commercial simulators for wells and pipelines are mainly validated for the flow of oil and natural gas, with extensions existing for pure CO_2 [6]. In a CCS context, it is necessary also to consider impurities, since pure CO_2 may not be optimal from a whole-chain perspective. Here, the label 'impurity' encompasses all non-CO_2 components, and some examples are methane, hydrogen, nitrogen and water. The CO_2 stream composition will be a function of the CO_2 source, the capture process and the purification and conditioning stages [7].

Small amounts of impurities are numerically more challenging to simulate than large amounts, due to the resulting narrow phase envelope. CO_2-brine mixtures constitute a further challenge for the simulation of CO_2-injection wells, because brine may flow back from the reservoir into the well during shut-in or blow-down. The flow model then needs to be able to handle two liquid phases, one CO_2-rich and one brine-rich, and possibly a CO_2-rich gas phase, along with the two-way coupling between well and near-well flow.

Even though normal operation may be virtually steady-state, dynamic situations will occur during shut-in, start-up, changes in the operating conditions or different undesired scenarios such as blow-out. The dynamics of the well flow is influenced by the response of the surrounding reservoir. This needs to be taken into account by applying appropriate boundary conditions at the wellbore perforation. Often the boundary conditions are formulated assuming a constant far-field reservoir pressure and permeability. In some cases, this could constitute too large a simplification.

An early contribution towards coupled wellbore–reservoir simulation was given by Hadgu *et al.* [8], where the reservoir simulator TOUGH was coupled to the wellbore simulator WFSA. The coupling was expressed through a productivity index relating the wellbore and reservoir pressures. A three-dimensional two-phase model with conservation of mass and energy was considered in the reservoir, while a one-dimensional steady-state thermodynamic equilibrium model was employed for the wellbore.

Pekot *et al.* [9] simulated CO_2-injection wells and concluded that two-phase flow should be considered as an operating possibility. Lu and Connell [10] presented a one-dimensional quasi-steady-state model for fluid flow in non-isothermal wells. Their approach was based on an averaged-flow model with the Peng and Robinson [11] equation of state (EOS), and with the further assumption that solubility of CO_2 in the water phase can be neglected. Flow in the reservoir was not considered, but injection into the reservoir was modelled by a local productivity index. A transient model based on

This is the accepted version of an article published in Greenhouse Gases: Science and Technology
http://dx.doi.org/10.1002/ghg.2035

a drift-flux model formulation was presented by Lu and Connell [12]. Sacconi and Mahgerefteh [13] simulated pressure and temperature transients for CO_2 injection into depleted natural-gas reservoirs. The outflow boundary condition was modelled by employing an empirical pressure-flow relationship.

A fully coupled (implicit) approach was developed by Livescu *et al.* [14] for a general-purpose reservoir model with applications to heating as a technique for enhanced oil recovery. A one-dimensional drift-flux model based on Shi *et al.* [15] with experimental data from Oddie *et al.* [16] was used to represent multi-phase flow in the wellbore. The wellbore-reservoir coupling was modelled by a source term represented by a well index. A black-oil formulation was employed, allowing for three components and three fluid phases. Earlier contributions with simpler wellbore models can be found in References [17–19].

A coupled simulator for CO_2 leakage and injection for geologic carbon sequestration was developed by Pan *et al.* [20, 21], Pan and Oldenburg [22] (T2Well/ECO2N). A standard multiphase Darcy flow model was used in the reservoir, while a one-dimensional drift-flux model based on Shi *et al.* [15], Oddie *et al.* [16], was used to model two-phase non-isothermal flow of CO_2–water mixtures in the wellbore. The models were integrated by assigning the wellbore and reservoir to two different subdomains, and using Darcy's law to model the flow terms at the interface between the perforated wellbore and the reservoir. This is in contrast to applying the deliverability option (well index) considered by Hadgu *et al.* [8]. Through numerical examples, Pan *et al.* [21] studied and discussed the validity of quasi-steady-state flow for realistic scenarios. Transient behaviour up to several hundred days was observed for a test problem of CO_2 injection into a depleted gas reservoir.

Feng *et al.* [23] studied a transient three-phase (gas-liquid-liquid) CO_2-leakage model, incorporating it into the T2Well code. The flow of CO_2-H_2O-NaCl was studied in the wellbore, but transients in the reservoir were not considered. It was found that a leakage of CO_2 mixed with water and brine can lead to complex transient flow in the well.

In [24] we considered single- and two-phase flow during blow-out and shut-in in vertical CO_2-injection wells. The flow was described by a one-dimensional two-fluid model with a new formulation of the mass transfer between the two phases. In [4] we studied the heat transfer through the different materials surrounding the vertical pipe, and the resulting thermal stresses. For intermittent injection scenarios for direct offshore ship offloading, we found that high thermal stresses could occur. Hence, either a continuous injection scheme should be adopted, or suitable well materials should be chosen.

In our previous work [4, 24], CO_2 injection into the surrounding reservoir was modelled by a constant injectivity index, but flow in the reservoir itself was not considered. In this paper, we extend the previous approach by computing the varying reservoir pressure and fluid mobility by solving a near-well flow model which is bi-directionally and dynamically coupled to the flow model of the well. Further, we employ thermodynamics models able to predict the occurrence of single-phase, two-phase gas-liquid and three-phase gas-liquid-liquid states for CO_2 with impurities including water. The whole injection well is considered, allowing the inflow boundary conditions to be specified at the wellhead.

Using this coupled approach, we demonstrate that the dynamics in the well depend strongly on the reservoir properties including porosity and permeability. We consider one 'open' reservoir (permeability 3000 mDa and porosity 0.3) and one 'tight' reservoir (permeability 300 mDa and porosity 0.15) to highlight these effects. Further, we

This is the accepted version of an article published in Greenhouse Gases: Science and Technology
http://dx.doi.org/10.1002/ghg.2035

consider a case where a small amount of water is co-injected with the CO_2, giving a separate water-rich phase. Such a scenario may be of interest for mitigation of salt precipitation. Finally, we employ our method to calculate several cycles of intermittent CO_2 injection, showing that the intermittency influences the form of the CO_2-propagation front and showing the different dynamics during shut-in and subsequent re-start of injection.

2. Models

In the present work, we employ a partitioned approach [see e.g. 25], in which the flow in the well and in the reservoir exist in separate computational domains. The well is modelled in its full length from the topside valve to the bottomhole valve, and may be further extended to include the riser to ship or platform, or a pipeline to the shore. The coupled approach has the advantage that we can employ numerical methods and discretization schemes that are adapted to each set of governing equations. Another advantage is that the coupling between well and reservoir can be modelled at whatever level of resolution one desires, up to the level of detailed simulations resolving the bottomhole valve and/or the specific geometry of the well completion. In this manuscript our emphasis is on demonstrating the methods, so for simplicity the coupling between the well flow and the reservoir flow is achieved through source terms, as described in the following.

Furthermore, we employ EOS-CG [26], a reference-quality thermodynamic equation of state (EOS) that is tailor made for mixtures of CO_2, water and other CCS-relevant fluids, for computing fluid properties and performing thermodynamic flash calculations in both well and reservoir. Especially for tighter reservoirs where pressure can vary strongly over time, simpler cubic EOSs may not give accurate predictions for fluid properties over the whole range of pressure and temperature.

2.1. Well-flow model

The well flow is modelled as one-dimensional, consisting of one or several phases, which in turn can consist of N chemical components (species). Mass and heat transfer to the reservoir, as well as friction and gravity, are accounted for by source terms. Viscous effects other than wall or interphasic friction are ignored. Equilibrium in pressure, temperature and chemical potential is assumed, but the phases can travel at different velocities. These assumptions yield a mass-balance equation for each component, a momentum-balance equation for the mixture, and a total-energy-balance equation for the mixture, as described in the following. For a mathematical background of two-phase flow modelling, see e.g. Drew [27].

$$\frac{\partial}{\partial t}\Big(\sum_\pi \alpha_\pi \rho_\pi z_{\pi j}\Big) + \frac{\partial}{\partial x}\Big(\sum_\pi \alpha_\pi \rho_\pi z_{\pi j} u_\pi\Big) = -\varrho_j, \quad j \in [1,\dots,N], \tag{1}$$

$$\frac{\partial}{\partial t}\Big(\sum_\pi \alpha_\pi \rho_\pi u_\pi\Big) + \frac{\partial}{\partial x}\Big(\sum_\pi \alpha_\pi \rho_\pi u_\pi^2\Big) + \frac{\partial P}{\partial x} = \rho_\mathrm{m} g_\parallel - \mathcal{F}, \tag{2}$$

$$\frac{\partial}{\partial t}\Big(\sum_\pi \alpha_\pi \rho_\pi \hat{e}_\pi\Big) + \frac{\partial}{\partial x}\Big(\sum_\pi \alpha_\pi \rho_\pi u_\pi (h_\pi + 1/2 u_\pi^2 + g\bar{y})\Big) = Q - h_\mathrm{m}\varrho_\mathrm{m}. \tag{3}$$

Herein, α_π is the volume fraction of phase π and $z_{\pi j} = \rho_{\pi j}/\rho_\pi$ is the mass fraction of component j in the phase π. ρ denotes density, P denotes pressure and u is the

This is the accepted version of an article published in Greenhouse Gases: Science and Technology
http://dx.doi.org/10.1002/ghg.2035

velocity. The total specific energy includes the internal, kinetic and potential energy; $\hat{e}_\pi = e_\pi + 1/2u_\pi^2 + g\bar{y}$, where g is the gravitational acceleration and $\bar{y}$ is the elevation. In the momentum equation, $g_\parallel$ is the gravitational acceleration component in the axial direction of the pipe. In the model, x and $\bar{y}$ are independent, but in this paper we only consider vertical flow and they will be aligned.

The enthalpy is $h_\pi = e_\pi + P/\rho_\pi$. The subscript m denotes (multi-phase) mixture quantities. For example, the mixture density is $\rho_\mathrm{m} = \sum_\pi \alpha_\pi \rho_\pi$ and the mixture enthalpy is $h_\mathrm{m} = \sum_\pi \alpha_\pi \rho_\pi h_\pi / \rho_\mathrm{m}$. Q is the heat flux transferred to the fluid through the pipe wall and $\mathcal{F}$ is the wall friction.

$\varrho_\mathrm{m} = \sum_j \varrho_j$ is the mass flow rate per volume from the well into the reservoir. This term will be nonzero in one or more cells where the coupling to the reservoir is active, and in the finite-volume method employed here, it is integrated over the cell volumes to give a mass flow rate in kg s^{-1}. Further details of how ϱ_j is computed for the coupled case are given in Section 2.4.

The slip, i.e., the difference between the phasic velocities, can be calculated using a semi-empirical algebraic relation. In the simulations presented in this paper, we use no slip ($u_\pi = u$) for simplicity.

2.1.1. Wall-friction model

The wall friction, $\mathcal{F}$, is calculated as follows.

$$\mathcal{F} = \begin{cases} f_\pi \dfrac{\dot{m}|\dot{m}|}{2\rho_\pi d_\mathrm{i}} & \text{for single-phase flow,} \\ f_\ell \dfrac{\dot{m}|\dot{m}|}{2\rho_\ell d_\mathrm{i}} \Phi & \text{for two-phase flow,} \end{cases} \tag{4}$$

where $f_\pi = f(Re_\pi)$ is the Darcy friction factor, $Re_\pi = |\dot{m}|d_\mathrm{i}/\mu_\pi$ is the Reynolds number for phase π, $\dot{m} = \rho u$ is the mass flux, and d_i is the inner pipe diameter. The coefficient Φ is an empirical correlation, which is used to account for two-phase flow, and it depends on various properties of both phases. Here we have employed the Friedel [28] correlation. Details of the calculation of the two-phase coefficient Φ, and also further discussion, can be found in References [29, 30]. In the case that two liquid phases are present in addition to a gas phase, the liquid phases are averaged before the Friedel correlation is applied.

2.1.2. Heat-transfer model

The heat flux per fluid volume, Q, accounts for radial heat conduction from the tubing to the fluid. It is given by

$$Q = \frac{2h_\mathrm{i}}{r_\mathrm{i}}(T_\mathrm{i} - T), \tag{5}$$

where r_i is the tube inner radius, h_i is the fluid-wall heat-transfer coefficient, T_i is the tube inner wall temperature and T is the fluid temperature. To calculate T_i, similarly to what was done by Aursand *et al.* [4], we assume that the temperature profile around the well is radially symmetric, and the axial heat conduction can be neglected. In this way, the heat transfer from the fluid to the tubing and the conduction from the tubing, through packer fluid, casing, annular fluid and cement to the formation is accounted for. See Aursand *et al.* [4], Munkejord and Hammer [31] for further details.

This is the accepted version of an article published in Greenhouse Gases: Science and Technology
http://dx.doi.org/10.1002/ghg.2035

2.1.3. Numerical solution

In our previous work [4], we employed a robust method [see e.g. 31, 32] able to accurately capture the pressure waves inherent in the flow model. Thus the time-step length of that method was limited by the Courant–Friedrichs–Lewy (CFL) stability criterion based on the the speed of sound, i.e., giving short time-step sizes. In the present work, we are interested in performing longer simulations, therefore it is desirable to be able to solve the equations using longer time steps. The method is briefly summarized in the following.

The governing equations (1)–(3) are discretized on a regular forward-staggered grid using a first-order upwind-type finite-volume method similar to the one discussed by Zou *et al.* [33]. The resulting discrete equation system can be written in the following form:

$$\boldsymbol{F}(\boldsymbol{U}) = \boldsymbol{0}, \tag{6}$$

where $\boldsymbol{U} = [\ldots, \boldsymbol{U}_{i-1}, \boldsymbol{U}_i, \boldsymbol{U}_{i+1}, \ldots]$ consists of the vector of unknowns in each cell, $\boldsymbol{U}_i$. Here we have chosen

$$\boldsymbol{U}_i = [z_{1,i}, \ldots, z_{N-1,i}, P_i, h_{\mathrm{m},i}, u_{i+1/2}]. \tag{7}$$

Herein, the subscript i denotes that the scalars are evaluated at the centre of the computational cell i, whereas the vectors (velocities) are evaluated at the cell face $i + 1/2$. $z_{j,i}$ is the mass fraction of component j in cell i. The mass fractions should sum to unity, giving a specification equation for the missing $z_{N,i}$.

The non-linear equation system (6) can be solved by a Jacobian-free Newton–Krylov method as discussed by Knoll and Keyes [34]. Here we employ the PETSc library [35, 36] using the `SNESNEWTONLS` method, which is a Newton-based nonlinear solver that uses a line search. Within this method, the BiCGStab (biconjugate gradient stabilized) method with SOR (successive over-relaxation) as a preconditioner are employed.

It may happen that the above procedure does not converge for certain time steps in the simulation. If so, for those time steps, we revert to a procedure employing the Newton-Raphson method with a finite-difference Jacobian and a line-search algorithm.

2.2. Reservoir model

In the reservoir we consider multiphase multicomponent flow through a porous rock under the assumption of negligible fluid momentum (Darcy flow). We employ the standard relative permeability approach such that for the fluid phases present, the relative permeability of each phase depends on the volume fraction (saturation) of the phase at each point. Furthermore, we assume that the permeability is isotropic, so that it can be written as a scalar, and we have neglected capillarity so that the pressures of each of the phases in contact with each other are equal. The permeability can be spatially varying in the present method, and cases with log-normal permeability distribution are investigated in Section 3.2. The assumption of isotropic permeability is simplifying and deemed reasonable for the cases we consider here – e.g. at the Utsira formation, the near-well region is isotropic [37]. Further, even when the anisotropy is significant, it can be challenging to obtain representative estimates of anisotropy from core samples or history matching [38, 39]. If desired, it is possible to incorporate anisotropy in the present method, assuming that one employs either a K-orthogonal grid or more advanced flux approximations that remain accurate and consistent on non-K-orthogonal grids [40].

This is the accepted version of an article published in Greenhouse Gases: Science and Technology
http://dx.doi.org/10.1002/ghg.2035

In the current work we consider systems of two components, CO_2 (c) and H_2O (w), and two phases, one CO_2-rich (c) and one water-rich (w). Subscript $j \in \{c, w\}$ refers to component, while subscript $\pi \in \{c, w\}$ refers to phase.

Under the above assumptions, the Darcy flux of fluid phase π, $\boldsymbol{w}_\pi$, is given by

$$\boldsymbol{w}_\pi = -K \frac{k_{r\pi}}{\mu_\pi} \left(\nabla P - \rho_\pi \boldsymbol{g} \right), \tag{8}$$

where K is the permeability, $k_{r\pi}$ is the relative permeability, μ_π is the phase viscosity, P is the fluid pressure, and $\boldsymbol{g}$ is the gravitational acceleration. In this equation, the density and viscosity will be provided by thermodynamic relations, while the relative permeability $k_{r\pi}$ is a function of the phase volume fraction α_π, as further described in Section 2.2.3.

We remark that incorporating capillary pressure in the thermodynamic property calculations [see e.g. 41] for the reservoir constitutes future work. This is due to the properties of the experimentally fitted reference EOSs (Section 2.3), which are highly accurate at equilibrium, but which do not have the appropriate extrapolation properties, as discussed by Aursand *et al.* [42]. The experimental vapour-liquid equilibrium data used to fit the EOS is obtained with a capillary pressure of zero, which complicates the issue further.

2.2.1. Mass balance

Fluid flow in the reservoir is governed by conservation of mass. Let m_j denote the mass of component j per reservoir volume. It can be expressed as a sum over the phases,

$$m_j = \phi \sum_\pi z_{j\pi} \rho_\pi \alpha_\pi, \tag{9}$$

where ϕ is the porosity. The mass-balance equation for component j is then given by

$$\frac{\partial m_j}{\partial t} + \nabla \cdot \left(\sum_\pi z_{j\pi} \rho_\pi \boldsymbol{w}_\pi \right) = \varrho_j. \tag{10}$$

where ϱ_j is the mass flow rate per volume of component j from the well into the reservoir, see Eq. (1) where the same source term appears with opposite sign. Further details of how ϱ_j is computed for the coupled case are given in Section 2.4. Due to the strong difference in viscosity between the phases, the Darcy fluxes of the two phases will have a significant difference in magnitude. Because of gravity effects, the phase Darcy flux vectors may also have different direction.

For the numerical solution it is convenient to recast the mass-balance equation (10) into a fractional flow formulation,

$$\frac{\partial m_j}{\partial t} = \nabla \cdot \sum_\pi \left(z_{j\pi} \rho_\pi f_\pi \left(\boldsymbol{w}_t - K \lambda_\omega \left(\rho_\pi - \rho_\omega \right) \boldsymbol{g} \right) \right) + \varrho_j, \tag{11}$$

where $\omega = w$ if $\pi = c$ and $\omega = c$ if $\pi = w$, and $f_\pi = \lambda_\pi / \lambda$ is the fractional flow.

2.2.2. Pressure equation

By combining the two mass-balance equations (10) (one for each of the components) and the closure relation $\alpha_c + \alpha_w = 1$, one may formulate the pressure equation,

$$\nabla \cdot \left(-K \lambda \nabla P + \left(K \lambda_c \rho_c + K \lambda_w \rho_w \right) \boldsymbol{g} \right) = \mathcal{S}, \tag{12}$$

This is the accepted version of an article published in Greenhouse Gases: Science and Technology
http://dx.doi.org/10.1002/ghg.2035

where the source term on the right-hand side is given by

$$\mathcal{S} = \frac{1}{(z_{ww}z_{cc} - z_{cw}z_{wc})}\left[\left(\frac{z_{ww}}{\rho_c} - \frac{z_{wc}}{\rho_w}\right)\varrho_c + \left(\frac{z_{cc}}{\rho_w} - \frac{z_{cw}}{\rho_c}\right)\varrho_w\right] + V_{\text{res}}/\Delta t, \tag{13}$$

The term in the parenthesis in (12) is the total velocity, $\boldsymbol{w}_t$,

$$\boldsymbol{w}_t = \boldsymbol{w}_c + \boldsymbol{w}_w = -K\lambda\nabla P + (K\lambda_c\rho_c + K\lambda_w\rho_w)\,\boldsymbol{g}, \tag{14}$$

and $\lambda_\pi = k_{r\pi}/\mu_\pi$ the phase mobility while $\lambda = \lambda_c + \lambda_w$ is the total mobility. There is no time-derivative in this equation because sound waves are neglected, and furthermore we have neglected terms involving $\nabla(\rho_\pi z_{j\pi})$ because these are assumed small. Due to the thermodynamic flash calculations that give density as a function of temperature and pressure, this formulation could lead to inconsistencies between fluid volumes and pore volumes. This is corrected using the approach of Acs *et al.* [43], via the term $V_{\text{res}}/\Delta t$ where V_{res} is the difference between the volume occupied by all phases in the cell and the available pore volume of the cell. Since the correction enters in the pressure equation, the change in volume gets distributed across the fluid phases according to their compressibility. The method is described further in Section 2.2.4.

In the presence of gravity, we split the solution of (12) in two steps, as the boundary conditions which are compatible with the two source terms (injection and hydrostatic contributions to pressure) may be different.

2.2.3. Relative permeability model

The relative permeability model is a closure relation that relates the Darcy flux of each phase to the volume fraction of the phase. There exist many classes of relative permeability models, and the choice of model and model parameters depends on the specific reservoir in question, the pressure and temperature, and the fluids present. Here we consider a generic reservoir and thus employ a fairly simple Corey-type relative permeability model that is quadratic in the water volume fraction,

$$k_{rc}(\alpha_w) = (1 - \alpha_{wn})^2\,, \tag{15}$$

$$k_{rw}(\alpha_w) = \alpha_{wn}^2. \tag{16}$$

Here α_{wn} is the normalized water volume fraction,

$$\alpha_{wn} = \frac{\alpha_w - \alpha_{wr}}{1 - \alpha_{wr} - \alpha_{cr}}, \tag{17}$$

where α_{wr} and α_{cr} are the irreducible water and CO_2 volume fractions, respectively. Throughout this work we use $\alpha_{wr} = \alpha_{cr} = 0.05$.

These irreducible volume fractions are typical features of porous media flow, where it is observed in experiments that if a rock specimen is initially filled with fluid A, and another fluid B flows through it, some residual amount of fluid A will be left in the rock even after very long time. This is due to trapping of the fluid phase in pores where there is no flow path out. When the volume fraction of one phase approaches the irreducible volume fraction, the Darcy flux of this phase approaches zero. It should be noted, however, that when we consider fluids that can dissolve in one another, such as water and CO_2, we can have further reduction in the volume fraction due to transport as a dissolved component in the other phase.

This is the accepted version of an article published in Greenhouse Gases: Science and Technology
http://dx.doi.org/10.1002/ghg.2035

2.2.4. Numerical solution of the reservoir model

We apply an implicit pressure explicit mass (ImPEM) solution approach as described by Doster *et al.* [44]. In the following, let superscript n denote the numerical solution at time t_n. The ImPEM algorithm can then be summarized as [44]:

1. Solve the pressure equation (12) using α_π^n, $z_{j\pi}^n$ and ρ^{n+1} to obtain p^{n+1}.
2. Compute phase velocities $\boldsymbol{w}_\pi^{n+1}$ and total velocity $\boldsymbol{w}_t^{n+1}$ from p^{n+1} and α_π^n.
3. Solve the transport equation (11) for m_j^{n+1}.
4. Calculate α_π^{n+1}, $z_{j\pi}^{n+1}$ and ρ^{n+1} by a thermodynamic flash calculation as described in Section 2.3.

In contrast with the ImPEM method of Doster *et al.* [44], we use a more detailed EOS, and further, we use the same time-step size for the pressure and transport equations.

It is known that the ImPEM scheme may lead to volume inconsistencies in the sense that the sum of the fluid volumes does not equal the actual pore volume in each cell. For an incompressible system this error can usually be neglected [44]. However, the thermodynamic flash calculation introduced in our approach complicates this matter, because the densities of the fluid phases are given by the temperature and pressure. When left uncorrected, we have observed a relative difference between pore volume and total fluid volume of up to 10% in cells close to the front between the two phases. To handle this discrepancy, the previously mentioned volume correction term is added to (12), following [43], which ameliorates the problem. When running simulations where the reservoir is coupled to the injection well, we have found that the correction needs to be distributed over several coupling intervals to avoid causing artificial pressure waves propagating in the well.

The pressure equation (12) and transport equation (10) are solved by finite-volume methods on a structured Cartesian grid. The pressure equation is solved every transport-equation time step, because most of the computational load is in the thermodynamic flash calculations.

The pressure equation is discretized with a standard two-point flux approximation (TPFA) scheme, see e.g., [45] for details. As this is a Poisson equation, it is elliptic and yields a (sparse) linear system of equations. This system is solved either directly by lower-upper (LU) factorization, or iteratively by a biconjugate gradient stabilized method (BiCGStab) preconditioned by a geometrically-agglomerated algebraic multigrid method (GAMG) provided by the PETSc library [35, 36].

For the transport equation (10) we use a standard upwind finite-volume discretization with explicit Euler time integration. For the simulation to be stable, the time step, Δt, must satisfy the condition

$$\Delta t \leq \frac{\phi |V_i|}{\mathcal{S}_i^{\text{in}} \max_{0\leq\alpha\leq 1}\{f'(\alpha)\}}, \tag{18}$$

where $|V_i|$ is the volume of cell i, $\mathcal{S}_i^{\text{in}}$ is the maximal volumetric flow rate into cell i, and f is the fractional flow function of water, $f(\alpha) = (k_{rw}(\alpha)/\mu_w)/\lambda(\alpha)$. Effectively, we take the minimum of $|V_i|/\mathcal{S}_i^{\text{in}}$ over all cells, and evaluate $\max_{0\leq\alpha\leq 1}\{f'(\alpha)\}$ numerically. This stability condition was derived in [45].

2.3. Thermophysical property models

In this work, a highly accurate equation of state (EOS) has been used, namely, the Helmholtz-type reference model for CO_2 systems, EOS-CG [26], from the TREND

This is the accepted version of an article published in Greenhouse Gases: Science and Technology
http://dx.doi.org/10.1002/ghg.2035

library [46]. The EOS-CG gives better predictions for liquid-phase densities compared to the more common cubic models, but at an elevated computational cost. The EOS is used to calculate what phases are stable, and the densities and energies of the existing phases.

The CO_2-rich liquid phase and the gas-phase thermal conductivity and dynamic viscosity are calculated using an extended corresponding-state method with propane as the reference fluid [47, 48]. The water viscosity is calculated from the correlation by Phillips *et al.* [49], while the water conductivity is calculated using the extended corresponding-state method.

In the well model, the mixture enthalpy, h_{m}, pressure, P, and the mixture component mass-fractions, z, are selected as variables. As a consequence, an enthalpy-pressure flash must be solved to find a stable phase distribution. Thus the fluid and thermodynamics are fully coupled, and phenomena like phase transition and expansion cooling (often called Joule-Thomson cooling) are accounted for.

The reservoir model is isothermal, and a similar temperature-pressure flash must be solved. The numerical schemes solving the global minimization flash problems are taken from Michelsen and Mollerup [50]. For the flash calculations we utilize our framework for calculation of thermodynamic properties [51]. In the reservoir calculations we employ tabulation of the fluid properties in order to reduce computational cost.

2.4. Well-reservoir interaction

Coupling of the reservoir model and the well flow model is realized through source terms expressing flow between the wellbore and the surrounding porous media. Such coupling conditions are commonly used, see e.g., [8, 10, 14, 19, 24]. The total flow rate from the well to the reservoir is expressed in terms of a well index Λ and the pressure drop from inside the wellbore to the injection point in the reservoir, $P_{\mathrm{wb}} - P_{\mathrm{R}}$, so that

$$\mathcal{S}_\pi = \Lambda_\pi (P_{\mathrm{wb}} - P_{\mathrm{R}})/\mu_\pi, \tag{19}$$

where $\mathcal{S}_\pi$ is the volume flow (m^3/s) of phase π. This is related to the mass flow rate per volume, ϱ_j, of component j, by taking the integral over the source term ϱ_j, cf. (1) or (10), yielding:

$$\mathcal{S}_\pi = \int_V \alpha_\pi/\rho_{\mathrm{m}} \sum_j \varrho_j \,\mathrm{d}V', \tag{20}$$

where the densities refer to the state in the reservoir at the beginning of the time step.

The well index Λ_π can be approximated by Peaceman's well model [52]. To take into account formation damage caused by drilling and perforation factors, a dimensionless skin factor, s, is commonly added to the well model, [see e.g. 53], so that

$$\Lambda_\pi = \frac{2\pi l_y K k_{r\pi}}{\ln\left(\frac{r_e}{r_w}\right) + s}, \tag{21}$$

where s can be estimated by various heuristic procedures [53], and depends on the specific completion chosen for the well, any stimulation performed, etc. In the cases considered here, the height l_y is 30 m, and we assume that the well is completed such that $\ln(r_e/r_w) + s = \pi$. With the mass flow rate given by this model, the corresponding volume flow is simply obtained by dividing by the density of the corresponding fluid phase. The total mass flow rate and the total volume flow rate are obtained by summing the contributions from each phase. We note again that for the reservoir model, the

This is the accepted version of an article published in Greenhouse Gases: Science and Technology
http://dx.doi.org/10.1002/ghg.2035

source term in the pressure equation is the volume flow. As the pressure drop from wellbore to reservoir is the same for both phases, the total volume flow can be written as

$$\mathcal{S} = \gamma(P_{\mathrm{wb}} - P_{\mathrm{R}}) \tag{22}$$

where the prefactor γ contains the sum of the productivity indices:

$$\gamma = \sum_{\pi} \alpha_{\pi}\Lambda_{\pi}/\mu_{\pi}. \tag{23}$$

If one considers a change in the volume flow, $\mathcal{S}$, into the reservoir, due to the elliptic nature of the Poisson equation, the result will be an instantaneous response in reservoir pressure, P_{R}. To enable stable sequential coupling of the well and reservoir flow, we apply a quasi-Newton approach, where the well model computes the linearized pressure response from the reservoir, using the sensitivity $\partial P_{\mathrm{R}}/\partial\mathcal{S}$ calculated numerically from the reservoir model. The volume flow ($\mathcal{S}$) out of the well then becomes linearly implicit in the reservoir pressure,

$$\mathcal{S} = \gamma\left(P_{\mathrm{wb}} - P_{\mathrm{R}} - \frac{\partial P_{\mathrm{R}}}{\partial\mathcal{S}}\left(\mathcal{S} - \mathcal{S}_0\right)\right) = \frac{\gamma\left(P_{\mathrm{wb}} - P_{\mathrm{R}} + \frac{\partial P_{\mathrm{R}}}{\partial\mathcal{S}}\mathcal{S}_0\right)}{1 + \gamma\frac{\partial P_{\mathrm{R}}}{\partial\mathcal{S}}}. \tag{24}$$

Furthermore, the relative permeabilities, $k_{r\pi}$, used to compute the productivity indices may change rapidly during the start of a simulation, because they are functions of the rapidly changing volume fractions at the well location, which again depend on the volume flow $\mathcal{S}$. For this reason, we employ an iterative scheme based on successive substitution of the productivity index until the value is within a certain tolerance of the value after completion of the well simulation step. These iterations are typically only performed in the initial steps of the simulation. The entire coupling scheme is illustrated in Figure 1 and outlined in Algorithm 1.

3. Results and discussion

In this section, we present results obtained by numerical solution of the models and the methods described in Section 2. First, we give some results from the well-flow model illustrating the effect of multiple components in the flow. We then present results from the coupled model for various cases, where we investigate the result from injecting into an open and a tight reservoir, respectively, and we consider the situations where gravity is neglected, where gravity is included, and where spatially varying permeability is also included. Furthermore, we study one case where a small amount of water is co-injected with the CO_2, in order to prevent formation water dry-out next to the well. Finally, we consider intermittent injection, e.g., from direct ship offloading, and the resulting dynamics in the well and reservoir.

3.1. CO_2-production well model validation study

Cronshaw and Bolling [54] presented experimental data for temperature and pressure in a CO_2-production well for various flow rates. We considered this case in Aursand *et al.* [4], but revisit it here to illustrate the effect of varying composition of the CO_2 stream. The case has been studied earlier, e.g., by Lu and Connell [10].

The Cronshaw and Bolling [54] data are for 97 % pure CO_2, where the remaining 3 % are not explicitly specified. However, Cronshaw and Bolling [54] indicate that

This is the accepted version of an article published in Greenhouse Gases: Science and Technology
http://dx.doi.org/10.1002/ghg.2035

Algorithm 1 Pseudocode of the coupling scheme.

while $t < t_{\text{End}}$ **do**
  $\Lambda^n \leftarrow \Lambda$ ▷ Initial guess for well index
  $\delta\Lambda \leftarrow 1$
  while $\delta\Lambda \geq \Lambda_{\text{tolerance}}$ **do** ▷ Iterate until well index is consistent
    $\frac{\partial P_R}{\partial S} \leftarrow \text{ReservoirSensitivity}(\mathcal{S})$ ▷ See line 28
    $\varrho \leftarrow \text{StepWellflowForward}(t, \Delta t, \Lambda^n, \frac{\partial P_R}{\partial S})$
    $\Lambda^{n+1} \leftarrow \text{StepReservoirForward}(t, \Delta t, \varrho)$
    $\delta\Lambda \leftarrow \Lambda^{n+1} - \Lambda^n$
  end while
  $t \leftarrow t + \Delta t$ ▷ Converged in Λ, accept solutions and continue to next time step
end while

procedure StepWellflowForward($t, \Delta t, \Lambda^n, P_R, \frac{\partial P_R}{\partial S}$)
  Update reservoir flow linearization parameters ($\Lambda^n, P_R, \frac{\partial P_R}{\partial S}$) ▷ Eqs. 23 and 24
  $X \leftarrow$ implicit solution of well flow equations at $t + \Delta t$ ▷ Eqs. 1, 2, 3 and 24
  $P_{\text{wb}} \leftarrow$ Value from X ▷ Get wellbore pressure
  $\varrho \leftarrow$ Computed from $P_{\text{wb}}, \Lambda^n, \frac{\partial P_R}{\partial S}$ ▷ Eq. 24
  return ϱ
end procedure
procedure StepReservoirForward($t, \Delta t, S$)
  Obtain P_R from solving $\nabla \cdot (-K\lambda\nabla P_R + \text{Buoyancy}) = \mathcal{S}$ ▷ Eq. 12
  Compute phase fluxes from ∇P_R, buoyancy and mobilities ▷ Eq. 8
  Obtain $z_{j\pi}$ from solving $\frac{\partial}{\partial t}\sum_\pi \phi\rho_\pi\alpha_\pi z_{j\pi} + \nabla \cdot \sum \text{Fluxes} = \varrho$ ▷ Eq. 10
  Obtain s_π, ρ_π, phase splits at $t + \Delta t$ from thermodynamic flash
  $\Lambda \leftarrow$ well index updated with new volume fractions and properties
  return Λ
end procedure
procedure ReservoirSensitivity(S)
  $\Delta S \leftarrow S \times 0.01$
  Obtain P_1 from solving $\nabla \cdot (-K\lambda\nabla P_1 + \text{Buoyancy}) = S$
  Obtain P_2 from solving $\nabla \cdot (-K\lambda\nabla P_2 + \text{Buoyancy}) = S + \Delta S$
  return $(P_2 - P_1)/\Delta S$
end procedure

This is the accepted version of an article published in Greenhouse Gases: Science and Technology
http://dx.doi.org/10.1002/ghg.2035

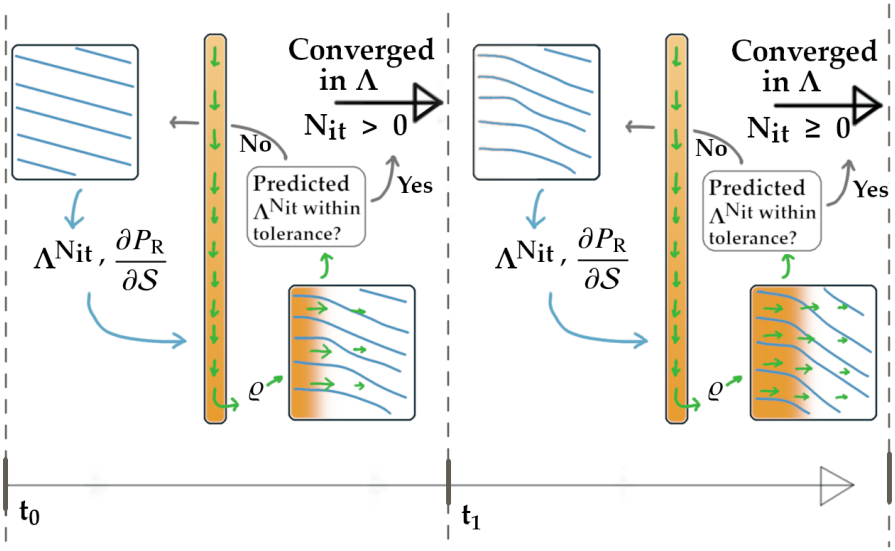

Figure 1: Illustration of the coupling scheme – blue lines indicate pressure contours in the reservoir, while yellow colour indicates the volume fraction of CO_2. We start with an initial guess on the well index, Λ^0, then run a coupled simulation step and evaluate the pressure and the fluid flow out from the well. Next, we calculate an updated well index, Λ^1, based on the current solution. If the new value is within an acceptable tolerance compared to the previous, we proceed to the next time step. If not, we iterate on $\Lambda^{N_{it}}$ until it converges.

Table 1: Parameters for model validation.

Quantity	Value
Well length	914.4 m
Deviation angle	26.5 degrees
Gravity along well axis	8.78 m s^{-2}
Tubing inner diameter	8.83 cm
Tubing roughness	4.572×10^{-6} m
Relative roughness	5.2×10^{-5}

water is produced at the wellhead and therefore must be a significant component. For this case we employ the EOS-CG [26]. For the water fractions considered here, EOS-CG predicts a separate water-rich phase. Hence liquid-liquid and vapour-liquid-liquid equilibra need to be handled. We note that for pure CO_2, EOS-CG is the same the EOS of Span and Wagner [55].

Cronshaw and Bolling [54] stated that after half a day of production (and maybe even earlier), the wellhead conditions no longer vary. This is because the heat transfer to the surroundings is much smaller than the (forced) heat convection in the fluid at this point. We therefore apply our model without any heat transfer to the surroundings.

Table 1 shows relevant parameters for the production well. In our calculations, the measured bottomhole pressure and temperature are used as inlet boundary conditions. The outlet pressure is set by an iterative procedure, such that the mass-flow rate matches the measured one. This procedure was chosen to produce results that can be compared directly with those of Aursand *et al.* [4], Lu and Connell [10]. The solution is integrated in time until steady state is reached. We remark that Cronshaw and Bolling [54] reported the flow rate in million standard cubic feet per day (Mscf/d). For clarity,

This is the accepted version of an article published in Greenhouse Gases: Science and Technology
http://dx.doi.org/10.1002/ghg.2035

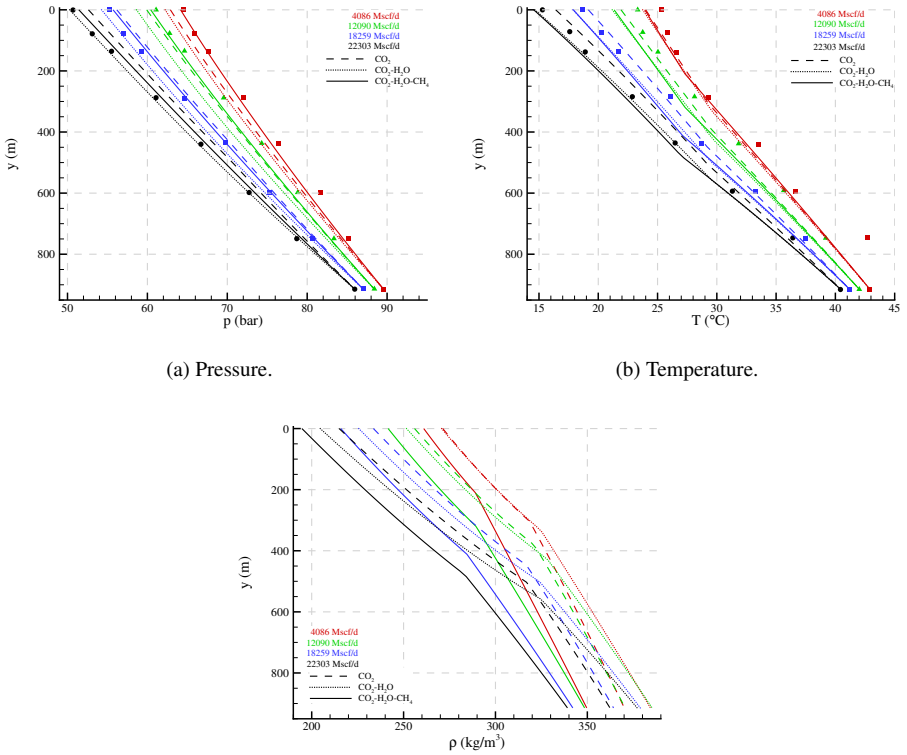

(a) Pressure.

(b) Temperature.

(c) Mixture density.

Figure 2: CO_2-production well: Our simulation results (lines) compared to measurements (filled markers) from Cronshaw and Bolling [54]. CO_2–H_2O denotes CO_2 with 3% H_2O. CO_2–H_2O–CH_4 denotes CO_2 with 2.5% H_2O and 0.5% CH_4.

we have kept this unit in the following figures. To obtain the mass-flow rate needed in our calculations, we converted the Mscf/d values using the EOS at 15 °C and 1 atm. For pure CO_2, this gives 2.5, 7.4, 11.2 and 13.7 kg s^{-1}.

Figure 2 shows our simulation results for pressure and temperature plotted along with experimental data. For pure CO_2, we obtain results that are very similar to those of Aursand *et al.* [4]. We have also plotted results obtained assuming a stream consisting of CO_2 with 3% water. As can be seen from Figure 2a, this gives a larger pressure drop, and a better fit to the data for the high flow rates, but a poorer fit to the low-flow-rate data. A third set of curves, calculated for CO_2 with 2.5% water and 0.5% methane, are also shown. It is interesting to note from Figure 2a that this gives a lower pressure drop for the lower flow rates, but a higher pressure drop for the higher flow rates, which results in a better overall agreement with the experimental data than for the case of pure CO_2. One important reason for this is shown by plotting the calculated mixture density in Figure 2c – it is sensitive to the stream composition and boundary conditions. For instance, if 3% water is replaced by 2.5% water and 0.5% methane, for the high-flow-rate case, the mixture density is reduced from 377 to 339 kg m^{-3} or about 10%.

For the temperature (Figure 2b), there is also good agreement with the experimental

This is the accepted version of an article published in Greenhouse Gases: Science and Technology
http://dx.doi.org/10.1002/ghg.2035

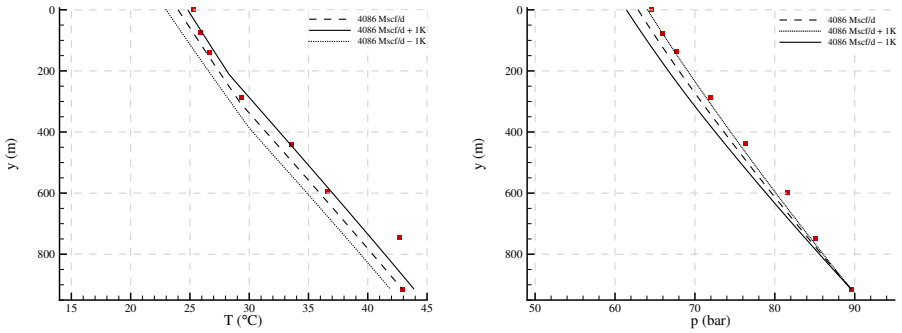

(a) Temperature.

(b) Pressure.

Figure 3: CO_2-production well, low-mass-flow case and pure CO_2: Impact on calculated temperature and pressure of a ±1 K perturbation of the inlet temperature.

data. Similarly to the case of pressure, the stream consisting of 3% water gives a higher temperature drop than that of pure CO_2. We observe, however, that the calculated temperature is less sensitive than the pressure to the inclusion of methane in the CO_2 stream. The temperatures calculated for a pure CO_2 stream have the lowest deviation for the two intermediate flow rates, whereas those for a stream consisting of CO_2 with 2.5% water and 0.5% methane have the lowest deviation for the highest and for the lowest flow rate.

A further observation regarding the temperature is given in Figure 3 for the low-flow-rate case for pure CO_2. The thermodynamic state in the well is relatively close to the critical point. Therefore, small perturbations in the boundary conditions can have significant effects. Here, we have run the case with a one-degree higher and lower temperature at the inlet. This gave a change in the pressure drop of -1.2 bar and $+1.5$ bar, respectively.

Cronshaw and Bolling [54] do not provide liquid mass-fraction data, but our simulation results in Figure 4a for pure CO_2 can be compared to theirs. In agreement with Cronshaw and Bolling [54], but in contrast to Lu and Connell [10], we obtain two-phase flow in the upper part of the well. For the highest flow rates, our calculated liquid mass fractions are similar to those of Cronshaw and Bolling [54], but for the lowest flow rate, we predict two-phase flow in a somewhat larger section of the well. In Figure 4b, we plot the liquid mass fraction for the case of CO_2 with 2.5% water and 0.5% methane. It can be observed that the gas fraction is smaller in this case. EOS-CG also predicts a separate water-rich liquid phase, containing most of the water. The liquid mass fraction of the water-rich phase is similar 'to plotting accuracy' for the four different flow rates.

To summarize, the Cronshaw and Bolling [54] is sensitive to boundary conditions, and also to the composition of the residual 3% of the CO_2 stream. By assuming CO_2 with 2.5% water and 0.5% methane we obtained better agreement with the pressure data, but no significant improvement with respect to temperature data compared to pure CO_2. The inclusion of water required the handling of a vapour-liquid-liquid equilibrium. Since parts of the well have a thermodynamic state close to the critical point, relatively small perturbations can give significant changes in the state. A further uncertainty not discussed here is the modelling of interphasic friction, which may play a

This is the accepted version of an article published in Greenhouse Gases: Science and Technology
http://dx.doi.org/10.1002/ghg.2035

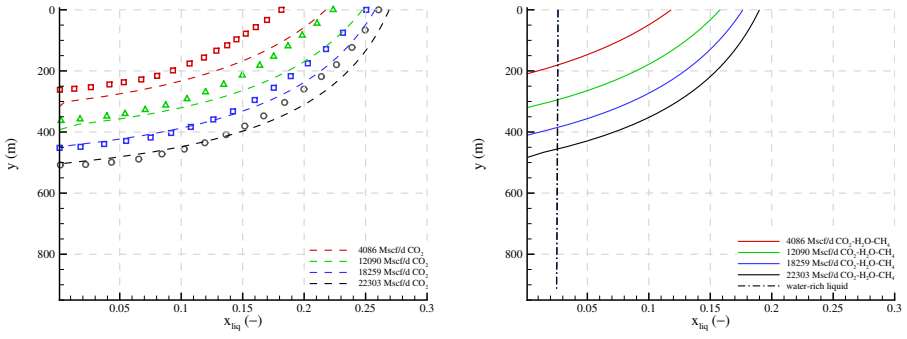

(a) Pure CO_2. (b) 97% CO_2–2.5% H_2O–0.5% CH_4.

Figure 4: CO_2-production well: Liquid mass fraction calculated for two fluid compositions, and compared to calculations from from Cronshaw and Bolling [54] (open markers).

Table 2: Injection-well parameters used for the case study.

Quantity	Value
Well depth	1500 m
Injection depth	1462.5 m
Formation level temperature	37 °C
Thermal gradient	24 °C km^{-1}
Gravity	9.81 m s^{-2}
Relative pipe roughness	5.2×10^{-5}
Well diameter	0.17 m

signficant role, especially in the part of the well containing both gas and liquid.

3.2. Coupled well-reservoir case study

In this section, we study the injection of CO_2 into a reservoir, with focus on well dynamics and effects in the reservoir near the well, employing the methodology described in Section 2.4.

3.2.1. Case description

We consider a vertical well of depth 1500 m coupled to an axially symmetric reservoir with a height of 30 m and radius 40 m. The well is discretized using an equidistant grid of 20 cells and the reservoir has an equidistant grid of 90 cells along the height and 120 cells along the radius.

The reservoir is connected to the centre of the bottom cell in the well, and the main well parameters are summarized in Table 2. This is comparable to the setup of Aursand *et al.* [4], except that we here employ a full near-well reservoir model instead of a simplified downhole boundary condition in the well.

For the rock properties, we consider Case A with porosity $\phi = 0.3$ and (average) rock permeability $K = 3000$ mDa, and Case B with porosity $\phi = 0.15$ and (average) rock permeability of $K = 300$ mDa. This corresponds to a very open reservoir (Case A) and a fairly tight reservoir (Case B), thus broadly spanning the range of flow features found in real reservoirs. For each of these two cases, we consider the situations a) where gravity is neglected and the permeability is uniform, b) where gravity is included

This is the accepted version of an article published in Greenhouse Gases: Science and Technology
http://dx.doi.org/10.1002/ghg.2035

and the permeability is uniform, and c) where gravity is included and the permeability varies according to a log-normal distribution with a mean of 3000 mDa and a standard deviation of 2000 mDa for Case A, and with mean and standard deviation equal to 300 mDa and 200 mDa, respectively, for Case B.

In the simulations, we employ the following boundary conditions. For the well, the inlet mass flow rate and enthalpy are specified, and the inlet pressure is implicitly calculated from the local well pressure, friction and hydrostatic pressure. The flow between the well and the reservoir is calculated from the pressure in the well and in the reservoir, according to (24). In order to calculate the heat transfer from the well fluid through the tubing, we assume a constant thermal gradient for the surrounding soil and rock.

The reservoir is initially filled with water at a temperature of 310 K. The boundary condition at $r = 0$ is no-flow as this corresponds to the axial singularity, while the injection is described by a source term that is evenly distributed over the cells covered by the well perforation. This simplification is made because even in the presence of gravity, the saturation in the innermost cells of the reservoir will be close to uniform in the vertical direction. More sophisticated models for the perforations and completion of the well and the vertical variation in flow rate might be considered in future work.

No-flow conditions are given at the top and bottom boundaries, while an outflow boundary condition together with a constant pressure of $P_{\text{bg}} = 150\,\text{bar}$ is specified at the middle of the outer boundary ($r = 40, z = 15$). As the coupling methodology is semi-implicit, the models can be run for more than one time step before exchanging information. In the following, we have used a coupling interval of 4 seconds in periods with transients such as start-up and shut-in, and 30 seconds otherwise. The coupling interval corresponds to a variable amount of time steps taken in the well and the reservoir models as the simulation progresses.

The well is initially at a shut-in condition in mechanical equilibrium with the reservoir pressure, and in thermal equilibrium with the vertical temperature profile of the surroundings. A constant thermal gradient of $0.024\,\text{K}\,\text{m}^{-1}$ is assumed for the formation (overburden and reservoir rock) enclosing the well. The temperature is set to be 2 °C at zero depth. As a consequence, the initial well pressure profile is given by the pressure of the pure CO_2 in the well generated by gravity analogous to a hydrostatic pressure profile.

At time $t = 0$, the flow rate at the wellhead is linearly increased from 0 to $50\,\text{kg}\,\text{s}^{-1}$ over a period of 600 s. The inlet pressure is extrapolated from inside the well based on the local friction and hydrostatic pressure contribution. The inlet enthalpy is set constant, to give a fluid temperature of approximately 5 °C. This is more robust than setting the temperature directly, in case there is phase change at the inlet.

The heat transfer between the well fluid and the surroundings is described using five thermal layers of different properties. We assume the same geometry and properties as in [4]. In particular, we assume that the casing is surrounded by drilling mud for the top 1400 m, while cement is used in the bottom 100 m.

3.2.2. Effect of gravity and rock properties

Reservoir dynamics. We first consider the situation where gravity in the reservoir is neglected. In this case, the front of CO_2 displacing water is uniform and follows a typical self-similar Buckley-Leverett profile with a shock immediately followed by a rarefaction wave.

In Figure 5, we show the CO_2 volume fraction, the pressure and the water Darcy flux for both Case A and Case B at various times. It is seen that for Case B with lower

This is the accepted version of an article published in Greenhouse Gases: Science and Technology
http://dx.doi.org/10.1002/ghg.2035

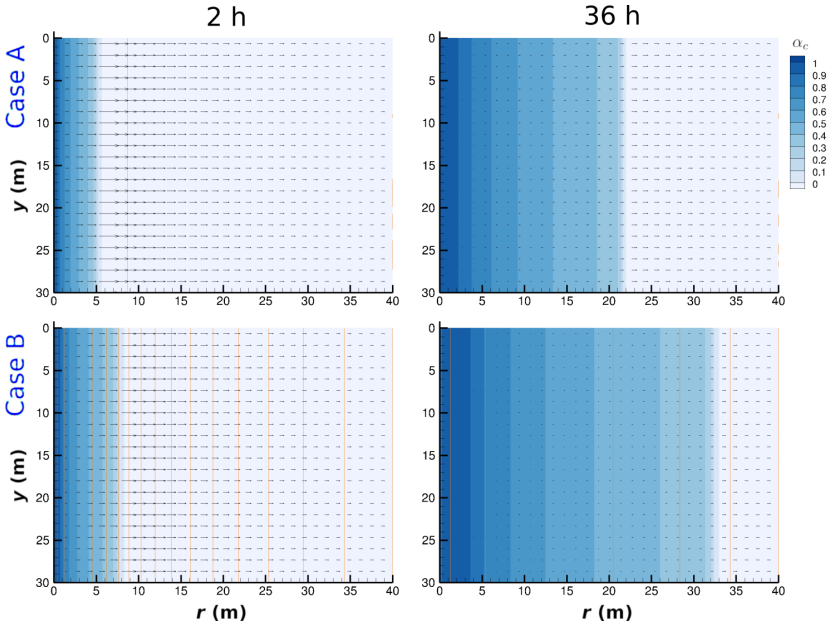

Figure 5: Coupled simulation with uniform porosity and without gravity in the reservoir. CO_2 volume fraction (blue), pressure (lines every 1 bar) and water Darcy flux (vectors shown at every 16th grid point), for Case A with porosity 0.3 and permeability 3000 mDa (top) and Case B with porosity 0.15 and permeability 300 mDa (bottom).

porosity, the invading front has proceeded farther out despite the lower permeability, because only half the pore volume is available. This results in a higher pressure drop as seen by the tighter pressure contours. Note that in the axisymmetric coordinate system used here, the volume of each cell increases linearly with r. It is also seen in this plot that the pressure contours are spaced much closer together in Case B, corresponding to the lower permeability.

In the situation where gravity is present and the rock permeability is uniform, we find that for Case A with the more open reservoir, the gravitational effect is significantly more pronounced than for Case B, as seen in Figure 6. This leads to the front of the invading CO_2 at the upper boundary in Case A almost catching up with Case B. For Case A, the buoyancy leads to the CO_2 preferentially flowing in the upper region of the domain, as the leading CO_2 edge has significantly higher mobility and thus the radial component of the pressure gradient is smaller in the region where CO_2 is already present. This is reflected in the pressure history at the well, because the presence of CO_2 farther out from the well decreases the pressure buildup more rapidly.

In the case where gravity is present and the rock permeability varies according to a log-normal distribution (Figure 7), we find that in Case A, the volume fraction of CO_2 overall resembles the situation with uniform permeability, while for Case B, some amount of viscous fingering is observed, where the smoothness of the invading CO_2 front is broken by the Saffman-Taylor instability.

Well dynamics. We now consider the effect of rock properties on the dynamics in the well. Figure 8 displays results for Case A-b, i.e., an open reservoir with gravity and uniform permeability. The pressure response is shown in Figure 8a, and the initial hydrostatic pressure at the top of the well is seen to increase after injection has started.

This is the accepted version of an article published in Greenhouse Gases: Science and Technology
http://dx.doi.org/10.1002/ghg.2035

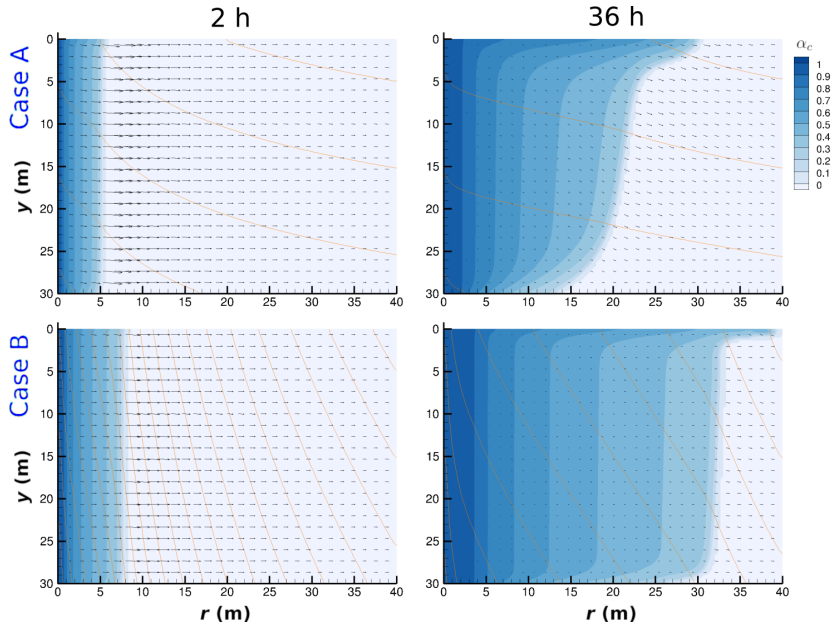

Figure 6: Coupled simulation with uniform porosity and with gravity in the reservoir. CO_2 volume fraction (blue), pressure (lines every 1 bar) and water Darcy flux (vectors shown at every 16th grid point), for Case A with porosity 0.3 and permeability 3000 mDa (top) and Case B with porosity 0.15 and permeability 300 mDa (bottom).

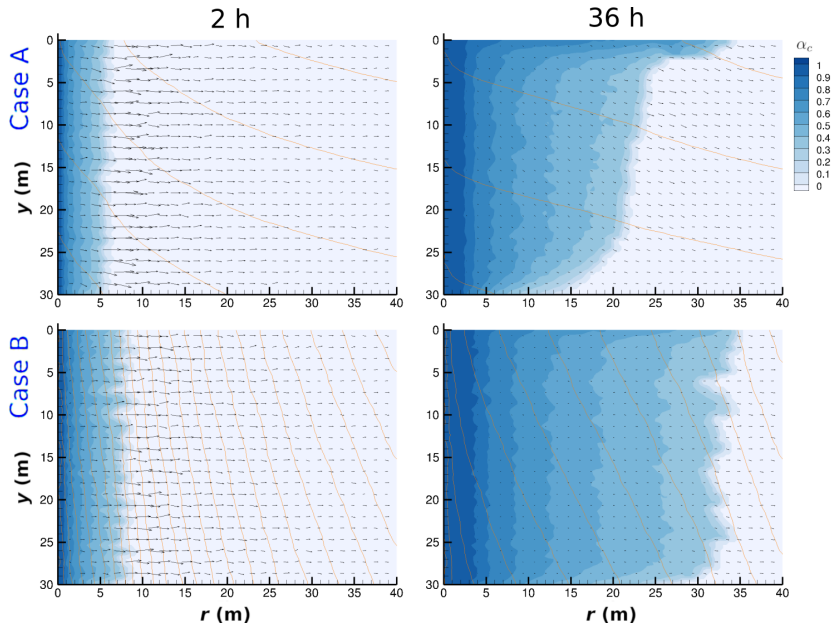

Figure 7: Coupled simulation with log-normal-distributed porosity and with gravity in the reservoir. CO_2 volume fraction (blue), pressure (lines every 1 bar) and water Darcy flux (vectors shown at every 16th grid point), for Case A with porosity 0.3 and average permeability 3000 mDa (top) and Case B with porosity 0.15 and average permeability 300 mDa (bottom).

This is the accepted version of an article published in Greenhouse Gases: Science and Technology
http://dx.doi.org/10.1002/ghg.2035

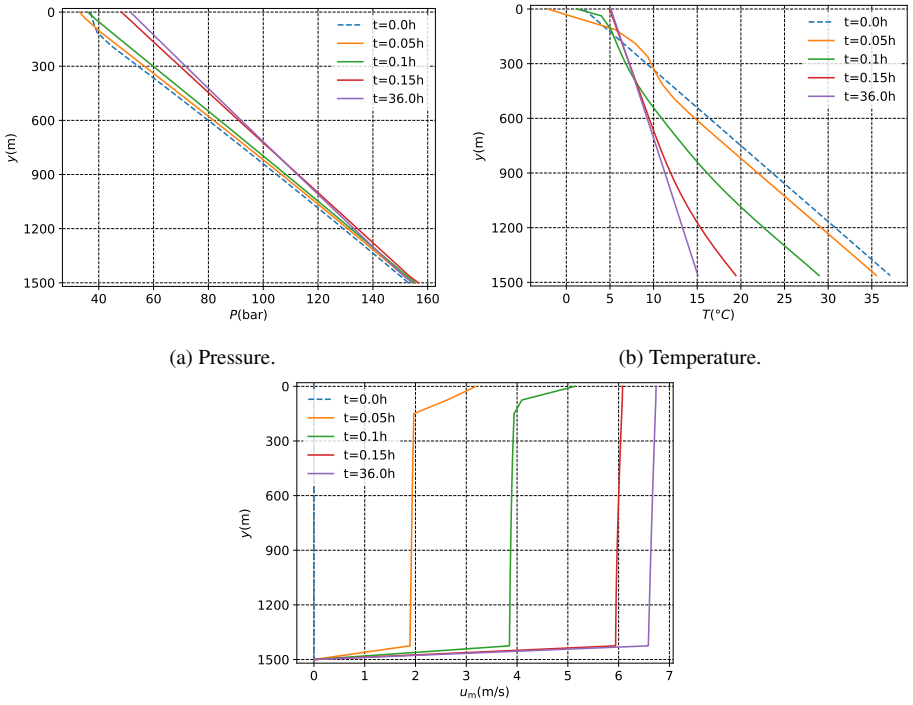

(a) Pressure.

(b) Temperature.

(c) Flow velocity.

Figure 8: Coupled simulation, Case A-b (open reservoir with gravity and uniform permeability). Time evolution of quantities in the well. The initial state is shown as a dashed blue line.

The rise is due to increased reservoir pressure, friction and changed density. Due to the permeable reservoir, the pressure response is small, and the well dynamics fade after 1 h. The well-fluid temperature is plotted in Figure 8b. Initially we observe thermal equilibrium with the surroundings, and a linear temperature profile. When fluid at an elevated temperature is being fed at the wellhead, a temperature front starts moving down the well. At the same time, the temperature at the bottom of the well decreases. This is due to the advection of colder fluid from the upper part of the well. Figure 8c shows the velocity of the well fluid. From initially being at rest, a flow velocity of approximately $6.7\,\mathrm{m\,s^{-1}}$ is stabilized within minutes, and remains relatively constant throughout the simulation. The flow is in a single-phase super-critical/liquid state for the entire simulation.

Figure 9 displays the time evolution of the pressure in the well for Case B-b, i.e., a tight reservoir with gravity and uniform permeability. The temperature and velocity dynamics are similar to Case A (Figure 8), but as the pressure response in the reservoir is much stronger, the well pressures are elevated in Figure 9 compared to Figure 8a.

To summarize, for the well dynamics, we find that the nature of the rock properties plays a significant role. In the case of the more permeable and open reservoir (Case A), the initial pressure transient is significantly smaller. In the less open and permeable reservoir (Case B), a larger transient as well as a higher ultimate bottomhole pressure is seen.

In addition to the effect of rock properties discussed above, gravity and spatially varying permeability also play a role. This means that the interplay between the well

This is the accepted version of an article published in Greenhouse Gases: Science and Technology
http://dx.doi.org/10.1002/ghg.2035

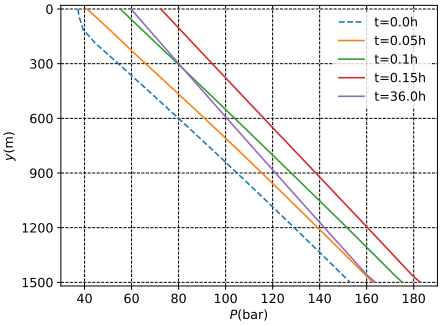

Figure 9: Coupled simulation pressure, Case B-b (tight reservoir with gravity and uniform permeability). Time evolution of pressure in the well. The initial state is shown as a dashed blue line.

and the near-well reservoir is significant for transient CO_2-injection operations, and that the specific details of the reservoir in question must be taken into account when studying the well dynamics. To illustrate this point, we plot in Figure 10 the bottomhole pressure dynamics normalized by the rock permeability K and the porosity ϕ, by considering the quantity

$$\tilde{P} = \frac{K[P - P_{\text{bg}}]}{\sqrt{\phi}}. \tag{25}$$

By normalizing in this way, we have incorporated the first-order effect of both porosity and permeability difference. For a one-dimensional well, one would divide by porosity to include the effect of reduced pore volume meaning that the CO_2 front travels farther in the same time, whereas for a cylindrically symmetric case, the appropriate reduction factor becomes $\sqrt{\phi}$. In all three cases, it is seen that the pressure dynamics are still different throughout the 36 hour duration, and furthermore that the inclusion of non-homogeneous permeability strongly affects the situation. In summary, one needs to consider the specifics of the well and the reservoir in question, and to simulate the coupled system in order to understand the transient dynamics of the injection operation.

3.2.3. Effect of downhole boundary condition

We will now compare the present coupled method to the simplified approach employed by, among others, Aursand *et al.* [4], using a constant injectivity and a constant reservoir pressure to specify the well bottomhole pressure. In Figure 11, the bottomhole pressure dynamics of coupled and non-coupled simulations, for Cases A-a and B-a, are compared.

For the non-coupled simulations, the reservoir pressure is set to

$$P_{\text{R}} = P_{\text{bg}} + (\mu_c/\mu_w) \max_t (P_{\text{coupled}}(t) - P_{\text{bg}}), \tag{26}$$

which is the steady-state pressure expected after long-term injection of CO_2. The background pressure, P_{bg}, is 150 bar. This gives a reservoir pressure of $P_{\text{R}}^{\text{A}} = 150.37$ bar for Case A, and $P_{\text{R}}^{\text{B}} = 152.79$ bar for Case B. The non-coupled simulations are run using a well index of $\Lambda_c^{\text{A}} = 1.7765 \times 10^{-10}$ m^3 for Case A and $\Lambda_c^{\text{B}} = 1.7765 \times 10^{-11}$ m^3 for Case B. These values are taken from the end of the corresponding coupled simulations, and the values force the bottomhole pressure to be close to constant during the non-coupled simulation. The non-coupled and coupled pressure responses observed in

This is the accepted version of an article published in Greenhouse Gases: Science and Technology
http://dx.doi.org/10.1002/ghg.2035

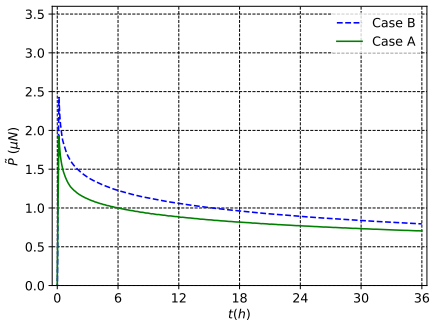

(a) Without gravity and with homogeneous permeability in reservoir.

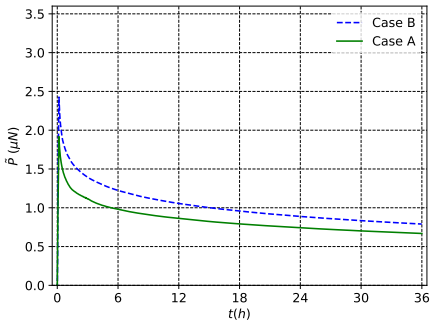

(b) With gravity and homogeneous permeability in reservoir.

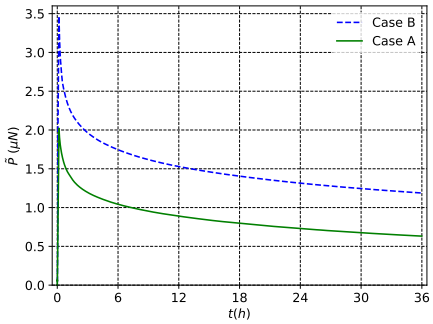

(c) With gravity and non-homogeneous permeability in reservoir.

Figure 10: Comparison of Case A and B bottomhole pressure dynamics. The pressure is shown as $\tilde{P} = K[P - P_{\text{bg}}]/\sqrt{\phi}$, which is scaled according to permeability and porosity. Despite this scaling, the bottomhole dynamics remain different.

This is the accepted version of an article published in Greenhouse Gases: Science and Technology
http://dx.doi.org/10.1002/ghg.2035

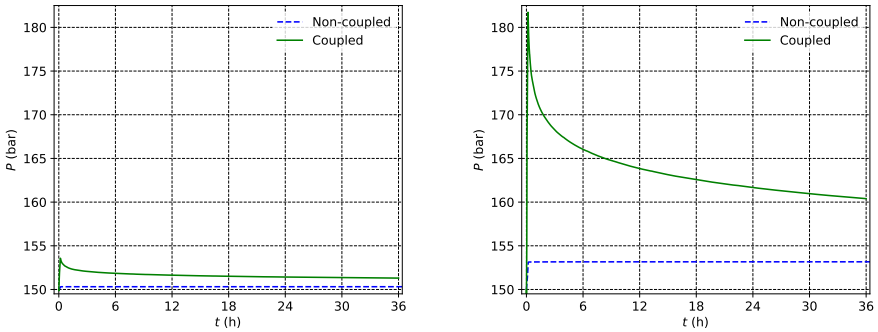

(a) Case A (open reservoir).

(b) Case B (tight reservoir).

Figure 11: Comparison of bottomhole pressure dynamics of coupled and non-coupled simulations for Cases A and B. The coupled simulations are run without gravity and with uniform reservoir permeability.

Figure 11, especially for Case B, give significantly different boundary conditions for the well simulation. This means that for the cases considered here, a coupled model is needed to capture the dynamics in the well.

The maximum bottomhole pressure observed in Figure 11 is due to a low total mobility when CO_2 starts to flow into the brine-filled reservoir. This is because a small volume fraction of CO_2 gives a very small relative permeability of CO_2, while the corresponding volume fraction of water becoming smaller than one gives a significant reduction in relative permeability of water. As more CO_2 is injected into the reservoir, the CO_2 can flow more easily, and we get a subsequent decrease in bottomhole pressure. We remark that Vilarrasa *et al.* [56] observed similar pressure behaviour in their numerical and semianalytical solutions, albeit at a larger temporal and spatial scale than what we consider here. Furthermore, Vilarrasa *et al.* [56] report that the magnitude of the pressure buildup is inversely proportional to the permeability of the reservoir. Our results agree with this observation.

3.2.4. Co-injection of water

We consider as an additional situation the co-injection of a small amount of water together with the CO_2. Salt precipitation due to injection of dry CO_2 dissolving residual water in the near-well region has been highlighted as a risk factor for CO_2-injection wells [see e.g. 57, and references therein]. Salt precipitation and the resulting loss of injectivity could mean that the well lifetime is reduced drastically. One possible solution for avoiding salt precipitation is to inject CO_2 that is already saturated with water, such that dry-out of residual water does not occur. Because the water solubility in CO_2 is a function of temperature and pressure, it is necessary to have a free water phase at the wellhead in order for the injected CO_2 to be water saturated. For this situation we use Case A with gravity and uniform permeability as a base case, and choose to study co-injection of 0.5% water (by mass) at the wellhead[1]. This yields a free water mass fraction of approximately 0.44% at the wellhead, decreasing to approximately 0.40% at the injection point, as shown in Figure 12. The pressure and temperature

[1] In the present injection scenario, this amount of water corresponds to 7.5 litres per minute, which is less than the demand of running a household water tap.

This is the accepted version of an article published in Greenhouse Gases: Science and Technology
http://dx.doi.org/10.1002/ghg.2035

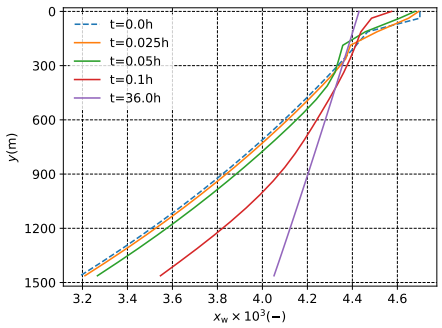

Figure 12: Free-water mass fraction for coupled Case A-b with co-injection of 0.5 % (by mass) at the well-head. The sudden change in free water close to the top of the well is due to a phase change in the CO_2-rich phase, and the corresponding difference in solubility.

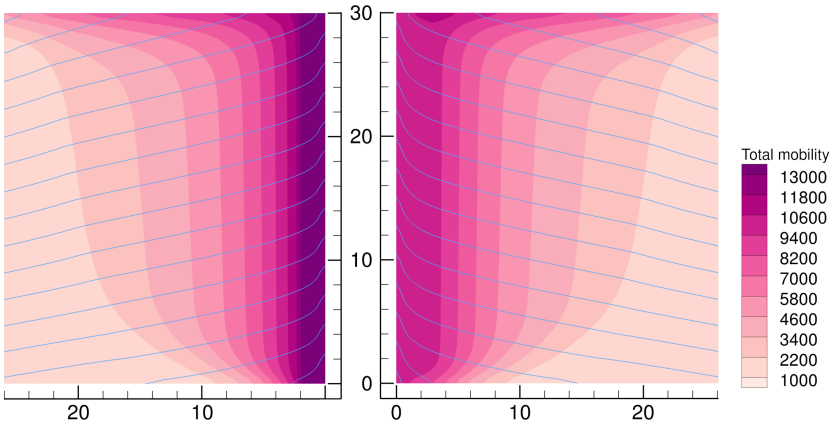

Figure 13: Coupled Case A-b, after 36 h of injection: Total mobility λ (magenta), pressure (blue lines every 0.2 bar). *Left:* base case with pure CO_2 injected. *Right:* injection of CO_2 saturated with water. For the cells close to the well, on the right of the left-hand-side plot, the dark region shows where the water has been completely dried out, while on the left of the right-hand-side plot, the residual (immobile) water volume fraction remains.

profiles are largely unaffected by this small amount of water co-injection (not shown). In Figure 13 we show the comparison of the reservoir pressure and the total mobility for the two situations. The dark region next to the well on the left-hand-side plot indicates where the CO_2 has dried out the residual water, thus salt precipitation would be likely to occur in this region. On the right-hand-side plot, it is seen that the injection of CO_2 already saturated with water does not dry out the residual water trapped next to the well. It is also seen that for these two cases, the pressure at the well differs only slightly.

We must emphasize here that we have employed a simple relative permeability model, and that we do not model the presence of salt. A quantitative investigation of water co-injection to reduce salt precipitation risks should be undertaken, using a more sophisticated relative permeability model taking into account *i.a.* the difference in flow resistance for saturated CO_2 with residual water present as compared to flow resistance for unsaturated CO_2 flowing through dry rock. Furthermore, to understand the effects of salt precipitation on the injectivity, it is necessary to consider where in the pore space

This is the accepted version of an article published in Greenhouse Gases: Science and Technology
http://dx.doi.org/10.1002/ghg.2035

salt is likely to precipitate, and how this affects the CO_2 phase distribution. The main conclusion from the present calculation is that co-injection of a small amount (0.5%) of water is sufficient to ensure that the CO_2 entering the reservoir does not dry out the residual formation water, and that this has negligible effect on the pressures observed in the well. Thus water co-injection holds promise as a salt-precipitation mitigation technique.

3.2.5. Intermittent injection

Our last example is an intermittent injection scenario. The case configuration is almost identical to Case A with uniform permeability and including gravity. The only differences are that we consider an intermittent injection scheme and that we increase the radial extent of our reservoir model from 40 to 60 meters. The total simulation time is set to 6 days (144 hours) with the following injection scheme:

- 0–24 hours: Pure CO_2 at rate $50\,\mathrm{kg\,s^{-1}}$
- 24–48 hours: No injection
- 48–72 hours: Pure CO_2 at rate $50\,\mathrm{kg\,s^{-1}}$
- 72–96 hours: No injection
- 96–120 hours: Pure CO_2 at rate $50\,\mathrm{kg\,s^{-1}}$
- 120–144 hours: No injection

The injection rate is ramped up linearly over a period of 600 s at each injection period. Similarly, at the beginning of each halt period, the injection rate is ramped down over 600 s.

The CO_2 volume fraction, pressure contours and water-phase volocity in the reservoir are displayed at different times in Figure 14. The results at 24 hours are identical to the previously studied case with constant injection rate (Figure 6) since these cases are equal at this point.

At 24.2 hours, there is a negligible change in CO_2 volume fraction, but the pressure lines are nearly horizontal, reflecting that the pressure is close to hydrostatic as the injection has stopped. Furthermore, we see that the water phase velocity has changed significantly and that water is pushing the CO_2 plume upwards at the lower part of the plume due to gravity.

After a period without injection (48 hours), we clearly see that the CO_2 plume has migrated upwards and the leading CO_2 edge has moved radially. Next, shortly after injection has started (48.2 hours) the pressure and velocity profile are altered again, and the plume starts to grow. Observe that the CO_2 plume has mostly grown in the upper part of the reservoir. This cycle repeats itself and the CO_2 plume moves radially, but mostly in the upper part. A constant injection scenario (Figure 6) gives a more evenly distributed CO_2 front. These intermittent simulations are run without volume correction, as the interaction between volume correction and well pressures during shut-in leads to spurious pressure waves. Further work is needed to develop a volume correction scheme that is robust when coupled with rapidly decreasing well flow conditions.

We also observe that we never get a counterflow of water into the well with this injection schedule. Further studies are needed to understand under what conditions one could expect this to happen. Rock and fluid properties, e.g., relative permeability, is likely to have an effect, and it is believed that having the reservoir continue below the injection well would increase the likelihood of counterflow. Finally, we also observe

This is the accepted version of an article published in Greenhouse Gases: Science and Technology
http://dx.doi.org/10.1002/ghg.2035

that the points where CO_2 saturation is non-monotonous as a function of time are limited to a region around the front in the lower half of the reservoir. This has important implications for issues such as salt precipitation, and should be studied in further detail.

The pressure and mass flow dynamics are shown in Figure 15. The overall evolution of pressure is as expected, with an elevated but decaying pressure during injection, and a value close to the reservoir boundary condition during the shut-in period. This pressure is not exactly equal to 150 bar, due to the buoyancy-driven flow in the reservoir during the shut-in period.

4. Conclusion

In this paper, we have presented a partitioned coupling approach to transient modelling of well and near-well reservoir flow of CO_2. Both the well and the reservoir flow modelling employs high-fidelity thermodynamics through flash calculations with accurate equations of state to predict quantities such as phase fractions, mutual solubilities and densities. In the partitioned coupling approach, the three codes (well, reservoir and thermodynamics) can be developed independently in the paradigms and programming languages suited to each task. For the well we employ a homogeneous equilibrium model and solve the resulting system of equations with a fully implicit method using the Jacobian-free Newton–Krylov method. For the reservoir, we employ an implicit-in-pressure, explicit-in-mass scheme where thermodynamic flash calculations are used in every cell at every time step to solve for the solubilities, densities and volume fractions of the fluids.

We have discussed the Cronshaw and Bolling [54] case of a CO_2-production well, and we illustrated that the 3% uncertainty in the composition of the CO_2 stream influences the results in a significant way. By assuming a stream consisting of 97% CO_2, 2.5% water and 0.5% methane, we obtained a better agreement with the experimental data than by assuming pure CO_2. This required taking a three-phase vapour-liquid-liquid equilibrium into account, enabled by our state-of-the-art thermodynamic framework. We employ reference quality equations of state that give accurate predictions of the fluid densities across the pressure range encountered, which would be challenging if the simpler cubic equations with volume shift were employed.

We have shown results for CO_2-injection scenarios in a open and a tight reservoir initially filled with water, and highlighted the effects of neglecting or including gravity in each case, as well as the effect of spatially varying rock permeability. For a given well depth with a fixed injection rate at the wellhead, we find that going from the open to the tight reservoir increases the peak bottomhole pressure by more than 20 bar. This also changes the temperature transients which the well materials are exposed to, as well as the flow velocities. For this case, a well-flow model without coupling to a near-well model would not be able to capture the well-flow dynamics.

Further, we examined a case where 0.5% (by mass) water is co-injected with CO_2, and demonstrated that this yields CO_2 that is saturated with water as it travels down the well and enters the reservoir, with negligible increase in well pressures, but eliminating the dry-out of residual water in the near-well region.

Finally, we demonstrated the calculation of multiple cycles of intermittent CO_2 injection. The cyclic injection led to the CO_2 flowing preferentially in the upper part of the reservoir to a larger degree than what was observed for constant injection. For the current parameters, we did not observe backflow of water into the well, and non-monotonous time evolution of CO_2 saturation was found only in a limited region of the near-well domain.

This is the accepted version of an article published in Greenhouse Gases: Science and Technology
http://dx.doi.org/10.1002/ghg.2035

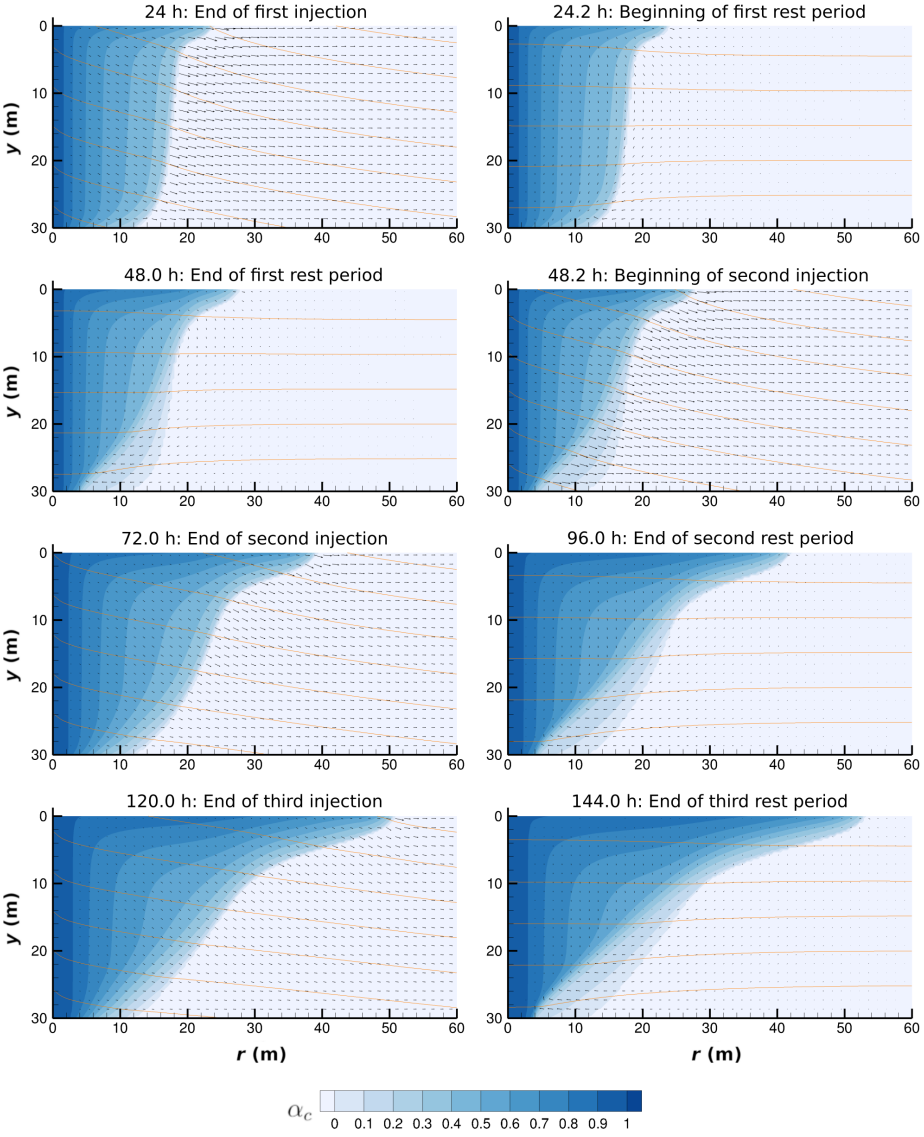

Figure 14: Case A with intermittent injection. CO_2 volume fraction (blue), pressure (lines every 1 bar) and water Darcy flux (vectors shown at every 16th grid point).

This is the accepted version of an article published in Greenhouse Gases: Science and Technology
http://dx.doi.org/10.1002/ghg.2035

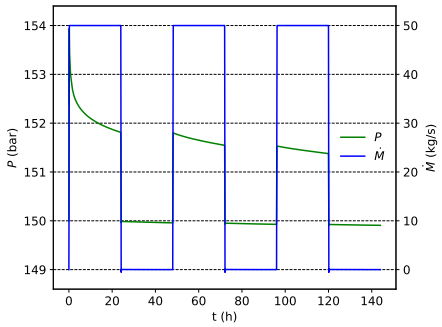

Figure 15: Bottomhole pressure and mass-flow dynamics of coupled simulations for Case A with intermittent injection. The simulations are run with gravity and with uniform reservoir permeability for 6 days. Pressure is plotted in green against the left y-axis, while mass-flow is plotted in blue against the right y-axis.

The present work demonstrates the utility of the partitioned coupling approach to the modelling of well and near-well reservoir flow, and it illustrates the potential of fluid flow models which are coupled with high-fidelity thermodynamics. Future work may extend this to account for thermal effects in the reservoir, as well as more sophisticated relative permeability models in the context of dry-out of the wetting phase and precipitation of salt.

Acknowledgements

ACT ELEGANCY, Project No 271498, has received funding from DETEC (CH), BMWi (DE), RVO (NL), Gassnova (NO), BEIS (UK), Gassco, Equinor and Total, and is cofunded by the European Commission under the Horizon 2020 programme, ACT Grant Agreement No 691712.

References

[1] Aspelund A, Mølnvik MJ, de Koeijer G. Ship transport of CO_2: Technical solutions and analysis of costs, energy utilization, exergy efficiency and CO_2 emissions. *Chem Eng Res Des* 2006; 84(9):847–855. doi:10.1205/cherd.5147.

[2] Vermeulen TN. Knowledge sharing report - CO_2 liquid logistics shipping concept (LLSC): Overall supply chain optimization. Tech. rep., Global CCS Institute, Anthony Veder, Vopak, 2011.

[3] de Koeijer G, Hammer M, Drescher M, Held R. Need for experiments on shut-ins and depressurizations in CO_2 injection wells. In: Dixon T, Herzog H, Twinning S, editors, *GHGT-12 – 12th International Conference on Greenhouse Gas Control Technologies*. University of Texas at Austin / IEAGHGT, Austin, Texas, USA: Energy Procedia, vol. 63, 2014; pp. 3022–3029. doi:10.1016/j.egypro.2014.11.325.

[4] Aursand P, Hammer M, Lavrov A, Lund H, Munkejord ST, Torsæter M. Well integrity for CO_2 injection from ships: Simulation of the effect of flow and material parameters on thermal stresses. *Int J Greenh Gas Con* 2017; 62:130–141. doi:10.1016/j.ijggc.2017.04.007.

[5] Munkejord ST, Hammer M, Løvseth SW. CO_2 transport: Data and models – A review. *Appl Energ* 2016; 169:499–523. doi:10.1016/j.apenergy.2016.01.100.

[6] Håvelsrud M. Improved and verified models for flow of CO_2 in pipelines. In: *The Third International Forum on the Transportation of CO_2 by Pipeline*. Gateshead, UK: Clarion Technical Conferences, 2012; .

[7] ISO. Carbon dioxide capture, transportation, and geological storage – cross cutting issues – CO_2 stream composition. TR 27921, International Organization for Standardization, Geneva, Switzerland, 2020.

[8] Hadgu T, Zimmerman RW, Bodvarsson GS. Coupled reservoir-wellbore simulation of geothermal reservoir behavior. *Geothermics* 1995; 24(2):145–166. doi:10.1016/0375-6505(95)91145-A.

[9] Pekot LJ, Petit P, Adushita Y, Saunier S, De Silva R. Simulation of two-phase flow in carbon dioxide injection wells. In: *SPE Offshore Europe Oil and Gas Conference and Exhibition*. Aberdeen, UK: Society of Petroleum Engineers, 2011; pp. 94–106. Paper SPE 144847.

[10] Lu M, Connell LD. Non-isothermal flow of carbon dioxide in injection wells during geological storage. *Int J Multiphase Flow* 2008; 2(2):248–258. doi:10.1016/S1750-5836(07)00114-4.

[11] Peng DY, Robinson DB. A new two-constant equation of state. *Ind Eng Chem Fund* 1976; 15(1):59–64. doi:10.1021/i160057a011.

[12] Lu M, Connell LD. Transient, thermal wellbore flow of multispecies carbon dioxide mixtures with phase transition during geological storage. *Int J Multiphase Flow* 2014; 63:82–92. doi:10.1016/j.ijmultiphaseflow.2014.04.002.

[13] Sacconi A, Mahgerefteh H. Modelling start-up injection of CO_2 into highly-depleted gas fields. *Energy* 2020; 191:116530. doi:10.1016/j.energy.2019.116530.

[14] Livescu S, Durlofsky LJ, Aziz K, Ginestra JC. A fully-coupled thermal multiphase wellbore flow model for use in reservoir simulation. *J Petrol Sci Eng* 2010; 71(3-4):138–146. doi:10.1016/j.petrol.2009.11.022. Fourth International Symposium on Hydrocarbons and Chemistry.

[15] Shi H, Holmes JA, Durlofsky LJ, Aziz K, Diaz L, Alkaya B, Oddie G. Drift-flux modeling of two-phase flow in wellbores. *SPE J* 2005; 10(1):24–33. doi:10.2118/84228-PA.

[16] Oddie G, Shi H, Durlofsky LJ, Aziz K, Pfeffer B, Holmes JA. Experimental study of two and three phase flows in large diameter inclined pipes. *Int J Multiphase Flow* 2003; 29(4):527–558. doi:10.1016/S0301-9322(03)00015-6.

[17] Stone TW, Edmunds NR, Kristoff BJ. A comprehensive wellbore/reservoir simulator. In: *Tenth SPE Symposium on Reservoir Simulation*. Houston, Texas, USA: Society of Petroleum Engineers of AIME, 1989; pp. 141–154.

[18] Stone TW, Bennett J, Law DHS, Holmes JA. Thermal simulation with multisegment wells. *SPE Reservoir Eng* 2002; 5(3):206–218. doi:10.2118/78131-PA.

[19] Pourafshary P, Varavei A, Sepehrnoori K, Podio A. A compositional wellbore/reservoir simulator to model multiphase flow and temperature distribution. *J Petrol Sci Eng* 2009; 69(1-2):40–52. doi:10.1016/j.petrol.2009.02.012.

[20] Pan L, Oldenburg CM, Wu YS, Pruess K. Wellbore flow model for carbon dioxide and brine. In: Gale J, Herzog H, Braitsch J, editors, *GHGT-9 – 9th International Conference on Greenhouse Gas Control Technologies*. MIT / IEA GHG, Washington DC, USA: Energy Procedia vol. 1, 2009; pp. 71–78. doi:10.1016/j.egypro.2009.01.012.

[21] Pan L, Oldenburg CM, Pruess K, Wu YS. Transient CO_2 leakage and injection in wellbore-reservoir systems for geologic carbon sequestration. *Greenh Gas Sci Tech* 2011; 1(4):335–350. doi:10.1002/ghg.41.

[22] Pan L, Oldenburg CM. T2Well—An integrated wellbore–reservoir simulator. *Comput Geosci* 2014; 65:46–55. doi:10.1016/j.cageo.2013.06.005.

[23] Feng G, Xu T, Tian H, Lu M, Connell LD, Lei H, Shi Y. Three-phase non-isothermal flow behavior of CO_2-brine leakage from wellbores. *Int J Greenh Gas Con* 2017; 64:183–193. doi:10.1016/j.ijggc.2017.07.009.

[24] Linga G, Lund H. A two-fluid model for vertical flow applied to CO_2 injection wells. *Int J Greenh Gas Con* 2016; 51:71–80. doi:10.1016/j.ijggc.2016.05.009.

[25] Degroote J, Bathe KJ, Vierendeels J. Performance of a new partitioned procedure versus a monolithic procedure in fluid-structure interaction. *Comput Struct* 2009; 87(11):793–801. doi:10.1016/j.compstruc.2008.11.013.

[26] Gernert J, Span R. EOS-CG: A Helmholtz energy mixture model for humid gases and CCS mixtures. *J Chem Thermodyn* 2016; 93:274–293. doi:10.1016/j.jct.2015.05.015.

[27] Drew DA. Continuum modeling of two-phase flows. In: *Theory of Dispersed Multiphase Flow. Proceedings of an Advanced Seminar*. Academic Press, NY, USA. ISBN 0-12-493120-0, 1983; pp. 173–190.

[28] Friedel L. Improved friction pressure drop correlations for horizontal and vertical two phase pipe flow. In: *Proceedings, European Two Phase Flow Group Meeting*. Ispra, Italy, 1979; Paper E2.

[29] Aakenes F. *Frictional pressure-drop models for steady-state and transient two-phase flow of carbon dioxide*. Master's thesis, Department of Energy and Process Engineering, Norwegian University of Science and Technology (NTNU), 2012.

[30] Aakenes F, Munkejord ST, Drescher M. Frictional pressure drop for two-phase flow of carbon dioxide in a tube: Comparison between models and experimental data. *Energy Procedia* 2014; 51:373–381. doi:10.1016/j.egypro.2014.07.044.

[31] Munkejord ST, Hammer M. Depressurization of CO_2-rich mixtures in pipes: Two-phase flow modelling and comparison with experiments. *Int J Greenh Gas Con* 2015; 37:398–411. doi:10.1016/j.ijggc.2015.03.029.

[32] Munkejord ST, Jakobsen JP, Austegard A, Mølnvik MJ. Thermo- and fluid-dynamical modelling of two-phase multi-component carbon dioxide mixtures. *Int J Greenh Gas Con* 2010; 4(4):589–596. doi:10.1016/j.ijggc.2010.02.003.

[33] Zou L, Zhao H, Zhang H. Application of Jacobian-free Newton–Krylov method in implicitly solving two-fluid six-equation two-phase flow problems: Implementation, validation and benchmark. *Nucl Eng Design* 2016; 300:268–281. doi:10.1016/j.nucengdes.2016.01.033.

[34] Knoll DA, Keyes DE. Jacobian-free Newton–Krylov methods: a survey of approaches and applications. *J Comput Phys* 2004; 193(2):357–397. doi:10.1016/j.jcp.2003.08.010.

[35] Balay S, Gropp WD, McInnes LC, Smith BF. Efficient management of parallelism in object oriented numerical software libraries. In: Arge E, Bruaset AM, Langtangen HP, editors, *Modern Software Tools in Scientific Computing*. Birkhäuser Press, 1997; pp. 163–202.

[36] Balay S, Abhyankar S, Adams MF, Brown J, Brune P, Buschelman K, Dalcin L, Dener A, Eijkhout V, Gropp WD, Kaushik D, Knepley MG, May DA, McInnes LC, Mills RT, Munson T, Rupp K, Sanan P, Smith BF, Zampini S, Zhang H, Zhang H. PETSc Web page. 2018. URL `http://www.mcs.anl.gov/petsc`.

[37] Zweigel P, Arts R, Lothe AE, Lindeberg EBG. Reservoir geology of the Utsira formation at the first industrial-scale underground CO_2 storage site (Sleipner area, North Sea). In: Baines SJ, Worden RH, editors, *Geological Storage of Carbon Dioxide*, *Special Publications*, vol. 233, pp. 165–180. London: Geological Society, 2004; doi:10.1144/GSL.SP.2004.233.01.11.

[38] Meyer R, Krause FF. Permeability anisotropy and heterogeneity of a sandstone reservoir analogue: An estuarine to shoreface depositional system in the Virgelle Member, Milk River Formation, Writing-on-Stone Provincial Park, southern Alberta. *B Can Petrol Geol* 2006; 54(4):301–318. doi:10.2113/gscpgbull.54.4.301.

[39] Chadwick RA, Noy DJ. History-matching flow simulations and time-lapse seismic data from the Sleipner CO_2 plume. In: Vining BA, Pickering SC, editors, *Petroleum Geology Conference series*, vol. 7. London: Geological Society, 2010; pp. 1171–1182. doi:10.1144/0071171.

[40] Lie KA, Krogstad S, Ligaarden IS, Natvig JR, Nilsen HM, Skaflestad B. Open-source MATLAB implementation of consistent discretisations on complex grids. *Computational Geosciences* 2012; 16(2):297–322. doi:10.1007/s10596-011-9244-4.

[41] Sandoval DR, Michelsen ML, Yan W, Stenby EH. VT-Based Phase Envelope and Flash Calculations in the Presence of Capillary Pressure. *Ind Eng Chem Res* 2019; 58(13):5291–5300. doi:10.1021/acs.iecr.8b05976.

[42] Aursand P, Gjennestad MA, Aursand E, Hammer M, Wilhelmsen Ø. The spinodal of single- and multi-component fluids and its role in the development of modern equations of state. *Fluid Phase Equilib* 2017; 436:98–112. doi:10.1016/j.fluid.2016.12.018.

[43] Acs G, Doleschall S, Farkas E. General purpose compositional model. *Soc Petrol Eng J* 1985; 25(4):543–553. doi:10.2118/10515-PA.

[44] Doster F, Keilegavlen E, Nordbotten JM. Multi-phase multi-component flow including capillary pressure and buoyancy: a robust implicit pressure explicit mass finite volume method. In: al Khuoury R, editor, *Computational Models for CO_2 Sequestration and Compressed Air Energy Storage*. Boca Raton, FL: CRC Press, 2014; .

[45] Aarnes JE, Gimse T, Lie KA. An introduction to the numerics of flow in porous media using Matlab. In: Hasle G, Lie KA, Quak E, editors, *Geometric Modelling, Numerical Simulation, and Optimization: Applied Mathematics at SINTEF*, pp. 265–306. Berlin, Heidelberg: Springer. ISBN 978-3-540-68783-2, 2007; doi:10.1007/978-3-540-68783-2_9.

[46] Span R, Eckermann T, Herrig S, Hielscher S, Jäger A, Thol M. TREND. Thermodynamic reference and engineering data 3.0. 2016. Lehrstuhl für Thermodynamik, Ruhr-Universität Bochum.

[47] Ely JF, Hanley HJM. Prediction of transport properties. 1. Viscosity of fluids and mixtures. *Ind Eng Chem Fund* 1981; 20(4):323–332. doi:10.1021/i100004a004.

[48] Ely JF, Hanley HJM. Prediction of transport properties. 2. Thermal conductivity of pure fluids and mixtures. *Ind Eng Chem Fund* 1983; 22(1):90–97. doi:10.1021/i100009a016.

[49] Phillips SL, Igbene A, Fair JA, Ozbek H, Tavana M. A technical databook for geothermal energy utilization. Tech. Rep. LBL-12810, Lawrence Berkeley National Laboratory, 1981.

[50] Michelsen ML, Mollerup JM. *Thermodynamic models: Fundamentals & computational aspects*. 2nd ed. Holte, Denmark: Tie-Line Publications, 2007. ISBN 87-989961-3-4.

[51] Wilhelmsen Ø, Aasen A, Skaugen G, Aursand P, Austegard A, Aursand E, Gjennestad MA, Lund H, Linga G, Hammer M. Thermodynamic modeling with equations of state: Present challenges with established methods. *Ind Eng Chem Res* 2017; 56(13):3503–3515. doi:10.1021/acs.iecr.7b00317.

[52] Peaceman DW. *Fundamentals of Numerical Reservoir Simulation*, *Development in Petroleum Science*, vol. 6. Amsterdam: Elsevier, 1977.

[53] Karakas M, Tariq SM. Semianalytical productivity models for perforated completions. *SPE Prod Eng* 1991; 6(1):73–82. doi:10.2118/18247-PA.

[54] Cronshaw MB, Bolling JD. A numerical model of the non-isothermal flow of carbon dioxide in wellbores. In: *SPE California Regional Meeting*. San Francisco, California, USA: Society of Petroleum Engineers, 1982; doi:10.2118/10735-MS. Paper SPE-10735-MS.

[55] Span R, Wagner W. A new equation of state for carbon dioxide covering the fluid region from the triple-point temperature to 1100 K at pressures up to 800 MPa. *J Phys Chem Ref Data* 1996; 25(6):1509–1596. doi:10.1063/1.555991.

[56] Vilarrasa V, Bolster D, Olivella S, Carrera J. Coupled hydromechanical modeling of CO_2 sequestration in deep saline aquifers. *Int J Greenh Gas Con* 2010; 4(6):910–919. doi:10.1016/j.ijggc.2010.06.006.

[57] Pruess K, Müller N. Formation dry-out from CO_2 injection into saline aquifers: 1. Effects of solids precipitation and their mitigation. *Water Resour Res* 2009; 45(3). doi:10.1029/2008WR007101.